Metabolic interaction models recapitulate leaf microbiota ecology

Journal Article

Author(s):
Schäfer, Martin; Pacheco, Alan; Künzler, Rahel; Bortfeld-Miller, Miriam; Field, Christopher; Vayena, Evangelia; Hatzimanikatis, Vassily; Vorholt, Julia A.

Publication date:
2023-07-07

Permanent link:
https://doi.org/10.3929/ethz-b-000621167

Originally published in:
Science 381(6653), https://doi.org/10.1126/science.adf5121

Funding acknowledgement:
668991 - Structure function relationships of the phyllosphere microbiota (EC)
-180575 - NCCR Microbiomes SNF (SNF)

This article was published in **Science** *on 7 July 2023, available at: doi.org/10.1126/science.adf5121*

Metabolic interaction models recapitulate leaf microbiota ecology

Authors: Martin Schäfer[1†], Alan R. Pacheco[1†], Rahel Künzler[1], Miriam Bortfeld-Miller[1], Christopher M. Field[1], Evangelia Vayena[2], Vassily Hatzimanikatis[2], and Julia A. Vorholt*[1]

Affiliations:

[1]Institute of Microbiology, ETH Zurich, Zurich, Switzerland.

[2]Laboratory of Computational Systems Biotechnology, École Polytechnique Fédérale de Lausanne, EPFL, Lausanne, Switzerland.

*Corresponding author. Email: jvorholt@ethz.ch.

†These authors contributed equally to this work.

Abstract: Resource allocation impacts the structure of microbiomes, including those associated with living hosts. Understanding the degree to which this dependency determines interspecies interactions may advance efforts to control host-microbiome relationships. Here, we combined synthetic community experiments with computational models to predict interaction outcomes between plant-associated bacteria. We mapped the metabolic capabilities of 224 leaf isolates from *Arabidopsis thaliana* by assessing the growth of each strain on 45 environmentally relevant carbon sources in vitro. We used this data to build curated genome-scale metabolic models for all strains, which we combined to simulate over 17,500 interactions. The models recapitulated outcomes observed in planta with over 89% accuracy, highlighting the role of carbon utilization and the contributions of niche partitioning and cross-feeding in the assembly of leaf microbiomes.

One-Sentence Summary: Interactions between plant microbiota members are recapitulated by experimentally informed genome-scale models.

Main Text:

Introduction

Various hosts, including animals (*1*, *2*), humans (*3*, *4*), and plants (*5*), support microbial communities with hundreds to thousands of different species. Recent studies have revealed that a deterministic relationship exists between environmental composition and community structure, even for complex microbiomes (*6–10*). Thus, a thorough understanding of the resources available to a community could enable prediction of its species and functional composition. Not only would the ability to make such predictions help us better understand the relationship between environment and phenotype, but it would also provide an accessible way to rationally design synthetic communities with defined functions.

Despite this potential, we still lack a comprehensive understanding of the information necessary to predict whether a specific organism will survive or be outcompeted in a particular environmental context. Resolving this question remains an active area of research, with studies that use interaction outcomes between pairs of organisms to predict overall community behavior representing a particularly attractive approach (*11–13*). Nonetheless, conducting the necessary mapping of possible interactions between all organisms remains experimentally challenging even for relatively simple communities, and largely out of reach for complex host-associated microbiomes in situ.

Given these limitations, one may ask which ecological concepts can be used to predict the role of individual organisms within a community context. Microbial populations are fundamentally bounded by resource availability, where limiting amounts of micronutrients such as carbon, nitrogen, and phosphorus act to constrain community size and lead to the emergence of competition between organisms (*14–16*). While the prevalence of these competitive interactions has begun to be quantified in a variety of ecosystems (*12*, *17–20*), the general rules by which they influence community-wide assembly patterns remain unresolved. As such, a commonly used approach is to infer the competitive potential between organisms using the degree of metabolic niche overlap between them, which relies solely on knowing their individual resource utilization capabilities (*21*, *22*). Though a resource-by-resource understanding of the metabolic profiles of complex microbiomes can be challenging to obtain, it represents a more accessible approach for inferring interspecies interactions and has proven successful at predicting high-level patterns of species diversity in communities (*10*, *23–26*).

Despite its benefits, the predictive power of niche overlap is limited in that it cannot account for the emergence of positive ecological interactions between organisms – either through resource partitioning, cross-feeding, orthogonal resource acquisition strategies, or evolved cooperation (*27–30*). As a complementary approach, genome-scale metabolic models present a tractable way to integrate the effects of these additional mechanisms into predictions of community structure (*31*, *32*). Genome-scale models are mathematical representations of the metabolic capabilities of individual organisms. They incorporate genes, reactions, and metabolites associated with a given organism's metabolic network, and are used to quantitatively assess how organisms can use available resources for growth (*32*). In addition to generating predictions of resource allocation for individual organisms, combinations of genome-scale models of different organisms have been increasingly employed to mechanistically describe pairwise and community-wide dynamics (*33–35*). Combining genome-scale models with predictions of niche overlap therefore presents a powerful way to predict interspecies interactions within microbiomes.

Here, we generated metrics of metabolic niche overlap and a collection of genome-scale models to predict interaction outcomes between 224 bacterial members of the *Arabidopsis thaliana* leaf microbiome. This environment, known as the phyllosphere, is an oligotrophic habitat where competitive interactions between its resident microbes are prevalent (*19*, *36*, *37*). Because it contains a variety of different carbon sources (*38*, *39*), it is an ecosystem that is well-suited for studying the effects of resource allocation on interspecies interactions and community structure. In particular, the exposed nature of the phyllosphere makes it a relatively accessible setting for study in controlled conditions. The microbiota of the phyllosphere has been shown to confer beneficial functions to the plant host (*40–42*), which, together with the scale of colonizable surfaces presented by plant leaves (*37*, *43*, *44*) and the economic significance of plant crops (*45*, *46*), underscores the importance of studying the processes underlying its assembly (*47*, *48*).

Results

Profiling the carbon source utilization capabilities of phyllosphere bacteria

Comprehensive collections of environmental strains are valuable resources for studying relevant host-microbe and microbe-microbe interactions (*42*, *49–52*). To examine interaction outcomes among members of the *Arabidopsis* phyllosphere (Fig. 1), we used the *At*-LSPHERE: a collection of 224 strains isolated from leaves of wild *Arabidopsis thaliana* plants that represent a cross-section of the taxonomic and functional diversity of the phyllosphere microbiota (*53*). We first assessed the ability of each strain to grow on minimal medium agar supplemented with individual carbon sources from a set of 45 (Table S1). These carbon sources – comprising a range of sugars, organic acids, sugar alcohols, one-carbon compounds, aromatic compounds, and amino acids – were selected based on the high prevalence of resources such as glucose, sucrose, and some amino acids that are known to account for a substantial fraction of carbon available to leaf epiphytes (*36*, *38*, *39*, *54*). These carbon sources were also selected in part based on the known ability of certain leaf strains to metabolize aromatic compounds, cleave glycosidic bonds, and/or utilize one-carbon compounds (*37*, *55*). In addition to these carbon sources, we supplemented the media with vitamins to enable the growth of auxotrophs (the set of carbon sources included amino acids, so we did not supply additional amino acids to the media). We used a plate assay to evaluate the growth of a given strain on a particular carbon source, which was compared to a carbon-free control, using both manual inspection and automated image processing (Methods).

Our in vitro metabolic screen revealed phylogenetically contingent patterns of carbon utilization capabilities across the *At*-LSPHERE collection (Fig. 2, Fig. S1). We found that strains belonging to the same genus displayed similar – or even identical – carbon source utilization profiles, suggesting trait conservation between closely-related species (Fig. 2A). We also identified genus-specific signatures of resource utilization, as well as cases in which strains were not able to grow on any of the tested carbon sources (e.g., *Chryseobacterium* and *Exiguobacterium*). These latter strains most likely have nutritional requirements that are not met by the minimal medium we provided (e.g., amino acid auxotrophies), as they were able to produce visible colonies on a complex medium (R-2A+M, Methods). In contrast, strains belonging to the genera *Arthrobacter*, *Pseudomonas*, and *Rhizobium* grew on a large number of carbon sources (27.5 ± 6.9, 27.1 ± 3.7 and 25.8 ± 3.6, respectively (mean ± s.d.)). To quantify these differences, we assigned a metric of substrate versatility, V, to each strain, defined as the percentage of all 44 growth-yielding carbon sources that each organism was able to utilize for growth (for this

analysis, methylamine was excluded as it did not support the growth of any strain). The most versatile strain was *Arthrobacter* sp. Leaf145 ($V = 77\%$), followed by *Pseudomonas* spp. Leaf15 and Leaf98, and *Rhizobium* sp. Leaf202 ($V = 73\%$, 70%, and 68%, respectively). When comparing the phylogenetic distribution of strain-specific versatilities, we observed that Beta- and Gammaproteobacteria had above average versatilities (Fig. 2B), while Actinobacteria (with the exception of *Arthrobacter*) and Bacteroidetes had below average versatilities. Finally, our screen revealed the presence of a canonical niche occupied by methylotrophs that was distinct from and smaller than that of many other strains (Fig. 2A, Fig. S2). Indeed, the lower average versatility of Alpha- and Betaproteobacteria, which respectively include *Methylobacterium* and *Methylophilus* spp., relative to Gammaproteobacteria reflects the low versatility of methylotrophs.

Our screen also revealed the varying degrees to which each resource promotes growth (Fig. 2C). To quantify these patterns, we assigned a measure of substrate fertility F to each tested carbon source, defined as the percentage of strains that was able to grow on that particular carbon source. The most fertile or commonly used carbon source was glucose ($F = 81\%$ of strains), followed by succinic acid ($F = 80\%$) and glutamate ($F = 78\%$) (Fig. 2C, Table S2). Among the most rarely used carbon sources were aromatic compounds including tryptophan ($F = 9\%$) and coniferyl alcohol ($F = 8\%$), a common component of lignin.

Given the largely orthogonal metabolic niche occupied by methylotrophs relative to all other strains, we repeated our calculations of substrate fertility without methylotrophs in order to more clearly detect patterns of fertility among the other substrates. This analysis revealed that mono- and disaccharides build a core set of carbon sources commonly used by the large majority ($F \geq 75\%$) of tested strains and the most fertile substrate, glucose, was consumed by 95% of the strains. The next most common group of carbon sources ($\geq 50\%$) included organic acids and amino acids that feed into the tricarboxylic acid (TCA) cycle (Fig. S3).

These experimentally determined carbon source utilization capabilities allowed us to calculate the degree of niche overlap among our strains. Here, we defined a niche overlap index (NOI) for each focal strain, A, with respect to any other strain, B, as the set of usable carbon sources shared by the focal strain and the competitor divided by the total number of carbon sources used by the focal strain (*23*, *56*), i.e.:

$$NOI_{A,B} = \frac{N_{CSources,\,AB}}{N_{CSources,\,A}}$$

We calculated NOI values for all pairs of strains, setting a threshold of 75% as likely prone to competitive exclusion (*57*) (Fig. 2D). In accordance with the similar carbon source utilization profiles, we found high niche overlap within most genera, suggesting frequent intra-genus competitive interactions. Additionally, we found methylotrophic strains to form two interconnected interaction spaces: one comprising *Methylobacterium* and the other *Methylophilus* strains, underscoring their degree of metabolic specialization compared to all other strains. Finally, members of the Microbacteriaceae had high niche overlap with a high number of other taxa, largely owing to their low versatilities. We also observed the opposite case: *Rhizobium* strains had a low NOI with other taxa, while essentially all strains (except Methylobacteria) had a high NOI with *Rhizobium* strains.

An *in silico* representation of phyllosphere bacterial communities

Having screened the carbon source utilization capabilities of the *At*-LSPHERE collection, we sought to model how these bacteria would interact metabolically in a leaf environment. To do this, we adopted a stoichiometric metabolic modeling approach because it allowed us to explicitly simulate strain- and substrate-specific patterns of resource utilization, conversion, and exchange in a multitude of defined environmental conditions. We thus began by creating draft genome-scale metabolic reconstructions (*58*) for each member of the *At*-LSPHERE. This process yielded a separate metabolic network for each of the 224 *At*-LSPHERE strains, containing all the metabolic reactions predicted to be contained by each organism based on its genome annotation. Upon generating these draft metabolic reconstructions, we used flux balance analysis (*31*) to simulate the growth of each one individually within a complete medium containing all 45 carbon sources used in our in vitro screen. We found that, while some of our reconstructions were predicted to produce biomass using this complete medium, the majority could not do so when only individual carbon sources were provided (Fig. 3A). While this inability to grow was at odds with our experimental results, it was not unexpected since models generated solely from genomic information are often missing key metabolic pathways and thus have limited predictive power without additional experimental curation (*33*, *59–61*). We therefore used the results of our carbon source screen to fill the apparent gaps in each metabolic reconstruction by using the tool NICEgame (*62*), which suggests biologically relevant alternative pathways to account for missing reactions by leveraging information on reaction thermodynamics. We followed this step with additional manual curation (Methods, Fig. S4), and then compared each of the resulting 224 models to their corresponding strains based on their ability (or inability) to utilize the 45 carbon sources used in our in vitro screen (Fig. S5). In sum, this process resulted in each genome-scale model having a final balanced accuracy of 0.98 ± 0.07 (Fig. 3A, mean precision 1, mean recall 0.96), with 214 models (96%) having a balanced accuracy of at least 0.85, and 189 models (84%) being 100% accurate.

Our curation process yielded a collection of 224 genome-scale models that revealed further metabolic capabilities and physiological characteristics of the *At*-LSPHERE collection (Fig. 3). The models contained between 1,568 (*Flavobacterium* sp. Leaf359) and 3,004 (*Pseudomonas* sp. Leaf15) reactions (Fig. 3B), which moderately correlated with the genome size of their corresponding strain ($R^2 = 0.54$, Fig. S6A). Reactions involved in the biosynthesis of glycerophospholipids, key components of the cell membranes of Gram-negative bacteria, were enriched in members of the Proteobacteria within our collection (Fig. 3C). We also found Firmicutes and Actinobacteria to contain more reactions related to degradation of plant polysaccharides (e.g., melibiose, raffinose, and sucrose) relative to other taxonomic classes, and identified an enrichment for benzoate degradation capabilities as previously reported in Betaproteobacteria (*63*, *64*). The high degree of similarity to our strains' known carbon source utilization capabilities was supported by a clustering analysis of the reactions contained in each model (Fig. 3D). Here, Methylobacteriaceae spp. and Methylophilaceae spp. formed clusters distinct from most other models, and *Acidovorax* strains clustered together with the majority of *Pseudomonas* and *Rhizobium* organisms. These clusters largely mirrored those generated from our in vitro data alone (Fig. 3E), which underscored the phylogenetic contingency of resource utilization patterns and may underlie the deterministic assembly of microbiomes in general. With this in silico representation of the *At*-LSPHERE collection, we proceeded to use our genome-scale models to simulate the ecological outcomes of mixed culture experiments.

Computational models recapitulate ecological patterns in planta

We assessed the predictive power of the genome-scale models and the NOI against experimental data in two in planta experiments (Fig. 4A, B). To do this, we inoculated *A. thaliana* seedlings with pairwise combinations of 7 bacterial strains, or with a community consisting of all 7 strains (referred to as SynCom7), and compared the colonization level of each strain in combination to the colonization density achieved in mono-association (Fig. 4B). To represent a range of metabolic capabilities, we selected strains across a gradient of substrate versatility values and hence a gradient of NOI. For the first experiment, we selected representative strains from the highly versatile *Arthrobacter* spp., *Pseudomonas* spp., and *Rhizobium* spp. (Leaf145, $V = 77\%$; Leaf15, $V = 73\%$; and Leaf202, $V = 68\%$; respectively), along with four additional strains with intermediate to low versatility values: *Rhodococcus* sp. Leaf233, *Sphingomonas* spp. Leaf34 and Leaf257, and *Microbacterium* sp. Leaf179 ($V = 55\%$, 36%, 45%, and 41% respectively). Based on NOI, we expected the strains with lower versatilities to more frequently decrease in abundance upon co-colonization with other strains, either in pairwise combinations or in a community context (Fig. 4C). However, all other strain pairings had low NOI values (< 75%), limiting the degree to which we could infer interaction outcomes for these combinations.

We used the genome-scale models corresponding to these seven strains to simulate their growth within an environment reflecting the carbon source availability of the *Arabidopsis* phyllosphere (Methods). As an indicator of the ecological outcomes of these pairings, we compared the predicted growth of each strain on its own with that in co-association with another organism: a strain was deemed to have experienced a negative interaction outcome if its biomass production rate in co-association was lower than that on its own, and a positive outcome if its biomass production rate was higher co-association. These simulations predicted an approximately even distribution of positive and negative outcomes for all seven organisms (Fig. 4C). However, when we considered the magnitude of the changes in growth experienced by each strain, we found that predictions skewed more strongly negative than positive. This observation is consistent with previous descriptions of the prevalence of competitive interactions in the phyllosphere (*18*, *19*), which suggests the commonality of exclusion of one strain by another. Indeed, when we compared the growth of each strain on its own to that in the presence of all six other strains, we predicted almost exclusively negative outcomes. Despite this overall distribution, we found that the number of positive or negative outcomes differed depending on the strain in question – with *Microbacterium* sp. Leaf179 and *Sphingomonas* sp. Leaf257 almost always experiencing a reduction in growth when paired with another strain. In contrast, *Rhizobium* sp. Leaf202, *Pseudomonas* sp. Leaf15, and *Arthrobacter* sp. Leaf145 were most often predicted to benefit from co-inoculation with another of our selected strains. These predicted positive outcomes corresponded to instances of low NOI values (Fig. 4C), suggesting that these strains could be able to metabolically evade competition by a partner strain and may additionally benefit from changes in the ecosystem (e.g., cross-feeding) induced by the partner strain.

The interaction outcomes of these seven strains in planta were largely congruent with those predicted by NOI and metabolic modeling. Of the outcomes that showed a fold change greater than 2 or less than 0.5, we found that a majority were negative, confirming the dominance of competition between these strains (Fig. 4D). In the SynCom7 condition, a significant abundance reduction was observed for all strains except for *Rhizobium* sp. Leaf202, matching our predictions and supporting the presence of increased competitive pressure in a community context. Our experimental data also highlighted the predictive power of NOI data alone for predicting interaction outcome directionality, with 93% of instances of negative outcomes

corresponding to an NOI greater than 0.75. Predictions generated by the genome-scale models yielded an increased degree of granularity, recapitulating the significant interaction directionalities we observed in planta with a balanced accuracy of 89% (Table S4, Table S5). These predictions additionally captured the weaker directionalities of border cases that did not meet our experimental cut-off, as seen in the positive interaction outcome for *Sphingomonas* sp. Leaf34 paired with *Microbacterium* sp. Leaf179, of *Arthrobacter* sp. Leaf145 paired with *Rhizobium* sp. Leaf202, and of *Rhizobium* sp. Leaf202 in the SynCom7 condition. These weakly positive effects occurred despite high predicted NOI, suggesting the influence of additional metabolic mechanisms not encompassed by competition.

We sought to further validate our predictions with a second set of pairwise and community experiments spanning more extreme degrees of niche overlap. Here, we generated pairings encompassing the two highly versatile strains *Rhizobium* sp. Leaf202 and *Arthrobacter* sp. Leaf145 ($V = 68\%$ and 77% respectively) as well as the low-versatility strains *Frigoribacterium* sp. Leaf8, *Curtobacterium* sp. Leaf154, *Rathayibacter* sp. Leaf164, and *Frondihabitans* sp. Leaf304 ($V = 27\%$ for all four strains). All pairings resulted in a high degree of niche overlap for the low-versatility strains, while the NOI for either Leaf202 or Leaf145 with any other strain was low. Correspondingly, the genome-scale models predicted almost exclusively negative interaction outcomes for all low-versatility strains, with weakly positive outcomes for Leaf202 in combination with all strains except Leaf145, as well as stronger positive outcomes for Leaf145 in combination with most other strains (Fig. 4E). We additionally predicted interaction outcomes for each of the three low-versatility strains paired with a combination of Leaf202 and Leaf145 (referred to as SynCom3), which resulted in strongly negative interaction outcomes for each strain. These predictions were tested via in planta experiments for these pairings: as predicted, all significant instances of log2 fold changes greater than 1 were negative, including those for each low-versatility strain in the SynCom3 condition (Fig. 4F). Additionally, Leaf202 and Leaf145 each experienced two instances of weakly positive outcomes when paired with other low-versatility strains, which were captured by our genome-scale modeling predictions. Taken together, our experiments confirmed the validity of the computational predictions (Table S4, Table S5) and highlighted the strong contribution of resource competition to strain-specific interaction outcomes in situ.

To test the specificity of our predictions to a leaf environment, we carried out a series of in vitro cultivations in which we cultured the same strain pairs and communities in shake flasks (Methods). These cultivations resulted in exclusively negative interaction outcomes for all strains in the SynCom7 and SynCom3 conditions (Fig. S7), similar to our in planta experiments. These outcomes, which are consistent with an additional set of community simulations using randomly selected strains (Fig. S8), highlight the increased degrees of competition that organisms may be subject to in multispecies settings. However, our in vitro experiments also resulted in substantially fewer positive outcomes of pairwise interactions when compared to in planta, suggesting competitive pressures inherent to batch cultures that are not captured by our use of NOI and genome-scale models. In particular, the lack of spatial structure may favor strains that experience fast growth when substrate availability is high, and thus outcompete slower-growing strains within the timescale of a batch experiment. Moreover, this rapid depletion of nutrients contrasts with the resource dynamics of leaf surfaces, which exhibit a steady resupply of resources that can be accessed by epiphytic microbes (*38*). Though we do not explicitly consider spatial structure in our use of NOI and genome-scale models, these tools generate predictions based on a broader consideration of the various resources that can be utilized by the organisms at steady state. This assumption may therefore better reflect a broader and more continuously

supplied pool of resources, which can be utilized by microbes on a population level in spatially structured settings.

Compensatory metabolic mechanisms offset resource competition

Beyond predicting interaction outcome directionalities, we used genome-scale modeling to explore the metabolic mechanisms that could be underlying the observed ecological patterns. We first examined experimentally validated interactions to determine changes in resource uptake rates that emerged as a result of pairing two strains together. As representative examples, we looked specifically at two interactions involving *Arthrobacter* sp. Leaf145, a highly versatile strain that experienced a weakly positive effect when paired with *Frigoribacterium* sp. Leaf8 and a negative effect when paired with *Rhodococcus* sp. Leaf233 (Fig. 4C-F, Fig. 5A). Our flux balance simulations had predicted that in both cocultures, Leaf145 would have a lower net uptake flux of sugars compared to those experienced in monoculture (Fig. 5B). This was also the case for Leaf8, which was additionally predicted to experience a reduction in amino acid uptake flux when paired with Leaf145. While a similar reduction in amino and organic acid uptake occurred for Leaf233, Leaf145 was able to take up amino acids at similar rates as in monoculture. The contribution of this re-allocation of resources to the dominance of Leaf145 can be seen in its interaction with Leaf8, in which Leaf145 is able to shift its metabolism to take up a slightly greater quantity of amino acids as in monoculture. The increased availability of these resources – in part a product of the low metabolic activity of Leaf8 – suggests metabolic cross-feeding as a contributing factor in the positive effect experienced by Leaf145 in coculture.

The emergence of distinct resource allocation patterns between these strain pairs prompted us to ask how widespread they could be across a wider ecosystem. We thus used the genome-scale models to generate predictions of pairwise interaction outcomes for all non-methylotrophic strains in the *At*-LSPHERE, carrying out a total of 17,578 pairwise simulations (Fig. 5C). These simulations revealed the high prevalence of competitive effects, with 63.2% of outcomes predicted to be negative (Fig. 5D). Of these, the large majority (representing 58.2% of all outcomes) were predicted to be strongly negative, which we defined as a strain's biomass production rate in coculture being less than 90% of that in monoculture. Conversely, 25.5% of all outcomes were predicted to be strongly positive (biomass production in coculture more than 110% that in monoculture), further underscoring the strength of competitive pressures within leaf bacterial communities. We combined these strain-specific effects to define interaction outcomes between pairs, which revealed that 94% of interactions involved at least one participant experiencing a negative outcome (Fig. 5E). As such, cooperative interactions were predicted to be relatively rare, with 3% of all pairwise interactions resulting in commensalism and only 1% resulting in mutualism.

An analysis of metabolic fluxes across our simulations revealed key differences in rates of resource uptake between positive and negative interaction outcomes (Fig. 5F). As expected, the models predicted significantly lower resource uptake rates for organisms that decreased in abundance relative to monoculture than for organisms that increased in abundance. However, while nearly all flux ratios associated with negative outcomes were below 1 (occurring for sugars, amino acids, and organic acids in 88.6%, 90.7%, and 78.4% of negative outcomes, respectively), many positive interaction outcomes displayed increases in amino acid and organic acid uptake flux (in 70.1% and 49.9% of positive outcomes, respectively). These patterns thus

suggest a stronger degree of competition for sugars among phyllosphere bacteria, which is more likely to be offset by increased uptake of amino and organic acids.

These predicted compensatory mechanisms suggested that strains with higher versatilities would be more likely to increase in abundance when in the presence of another strain. Indeed, strains with very high versatilities (e.g., *Acidovorax* spp. and *Pseudomonas* spp.) were predicted to have higher than average rates of experiencing positive outcomes (Fig. S9). However, strain-specific versatility itself was a poor predictor of positive outcome frequency ($R^2 = 0.10$), as strains with very low versatilities (e.g., *Chryseobacterium* spp., which did not grow on any of the supplied carbon sources individually, or *Bosea* sp. Leaf344) were also predicted to experience strongly positive outcomes in rare cases. These effects suggest a role of cross-fed amino or organic acids as valuable sources of metabolic complementation (*65*), which in addition to enabling highly versatile strains to outcompete a partner strain, can also facilitate the survival of specialized organisms.

Discussion

Understanding the factors that contribute to the assembly of microbiomes remains a challenge for the study of natural ecosystems. Here we have shown how predictions based on the resource utilization capabilities of individual bacteria enable recapitulation of interaction outcomes observed in the phyllosphere. These predictions underscored the prevalence of competitive interactions between leaf strains. Additionally, their high accuracy (Fig. 4) suggested that competition for resources is responsible for many outcomes observed in situ, as also recently observed in community contexts (*19*). In particular, our experiments showed how high degrees of niche overlap were reliably predictive of negative interaction outcomes in planta. This relationship demonstrates the role that highly versatile organisms play in communities, as well as the implications for the design of microbial consortia based on cooperative interactions, where pairings of highly competitive organisms can be avoided with greater certainty. Our work highlights how a resource-by-resource understanding of an organism's catabolic potential in monoculture is sufficient for making high-level predictions of competition in an ecologically relevant setting.

Beyond cataloging the metabolic capabilities of a large strain collection at high resolution, our in vitro carbon source screen informed the curation of genome-scale metabolic models for each of the 224 strains. Our experimentally curated collection of genome-scale models allowed us to go beyond the potential of niche overlap by predicting positive interaction outcomes and suggesting their molecular mechanisms. Our curation process provided a quantitative basis for the need to incorporate experimental data into model generation, given the low accuracy of the initial draft models based on genome annotations alone. While improved annotation resources, as well as organism-specific biomass compositions, may serve to reduce this source of uncertainty (*60*, *61*), we expect experimental curation to remain essential for selecting the optimal combination of gap-filled reactions to recapitulate an organism's exact resource utilization profile.

Our metabolic modeling predicted interaction outcomes based on carbon source utilization capabilities. Further curation that integrates additional properties such as vitamin auxotrophies and storage (*66*), as well as metabolic shifts occurring from gene regulation (*67*, *68*), is likely to improve the quantitative predictive power of this framework (*33*, *69*). Moreover, while our predictions based on metabolic mechanisms are informative of key aspects underlying the assembly of plant-associated microbiomes, they do not consider additional factors that are

known to shape leaf communities such as signaling molecules, antagonistic interactions, or host immunity (*5*, *70–73*). A potential consequence of this limitation may be seen in the example of *Pseudomonas* sp. Leaf15, which experienced a strong negative interaction in planta when paired with *Rhizobium* sp. Leaf202 (Fig. 4C, D). While this outcome was qualitatively predicted by our simulations, the presence of a type VI secretion system in Leaf202 previously described to be active against a *Pseudomonas* strain (*42*) may also be producing an additional inhibitory effect not captured in our modeling framework. Moreover, while our experimental approach that quantified community composition based on bulk sampling aligns with our use of flux balance analysis, it abstracts away the influence of spatial structure on interaction outcomes. Leaf surfaces are known to exhibit significant nutrient heterogeneity, which, together with the aggregation of microbes around leaf pores or in microdroplets, are likely to affect interaction directions at the microscale (*36*, *74*, *75*). Capturing varying degrees of uncertainty in our modeling predictions can partially represent this heterogeneity (Fig. S10), but an improved understanding of the nutrient compositions at specific locations on the leaf may enable future parametrization of existing metabolic modeling tools that can explicitly consider spatial structure (*76–79*).

Our present results underscore the strengths of an integrated approach for generating ecological predictions in a mechanistic yet scalable way, while establishing a computational resource for further exploration of the molecular mechanisms that underlie the assembly of complex microbiomes.

Materials and Methods

Cultivation of bacteria

At-LSPHERE strains were grown on R-2A agar (Sigma-Aldrich) supplemented with 0.5% (v/v) methanol (R-2A+M) at 22°C. Strains were routinely streaked out from a cryo stock stored at -80°C, grown for 4 days, streaked on fresh R-2A+M plates and grown for three more days prior to the start of experiments. If necessary, streptomycin (20 μg mL^{-1}) was added to the medium for selection.

Carbon source screen

The minimal medium agar plates were prepared with a common minimal medium composition (*83*). One liter of the final medium contained 2.4 g K_2HPO_4, 1.08 g $NaH_2PO_4 \cdot 2H_2O$, 1.62 g NH_4Cl and 0.2 g $MgSO_4 \cdot 7H_2O$ and 15 g noble agar (Becton, Dickinson and Company). The medium was supplemented with the following trace elements: 15 mg $Na_2EDTA \cdot 2H_2O$, 3 mg $FeSO_4 \cdot 7H_2O$, 4.5 mg $ZnSO_4 \cdot 7H_2O$, 3 mg $CoCl_2 \cdot 6H_2O$, 0.64 mg $MnCl_2$, 1 mg H_3BO_3, 0.4 mg $Na_2MoO_4 \cdot 2H_2O$, 0.3 mg $CuSO_4 \cdot 5H_2O$ and 3 mg $CaCl_2 \cdot 2H_2O$ and vitamins: 500 μg D-pantothenic acid hemi calcium salt, 100 μg biotin, 400 μg riboflavin, 400 μg thiamine HCl, 200 μg pyridoxal HCl 150 μg p-amino benzoic acid, 200 μg cobalamin, 50 μg lipoic acid, 150 μg nicotinic acid and 100 μg folic acid. All media components were prepared with Milli-Q® quality water (Millipore). Each carbon source was added as a 10x stock solution to the premixed medium, except for coniferyl alcohol and tyrosine, which were added to the medium directly as powder. The concentration of each carbon source was normalized to 30 mM carbon (e.g., 5 mM glucose and 30 mM methanol). A list of all 45 carbon sources and final concentrations can be found in Table S1.

At-LSPHERE isolates grown on R-2A+M medium were suspended (1 µL loopful) in 1 mL 10 mM magnesium chloride solution, which corresponds to an optical density at 600 nm (OD_{600}) of approximately 0.1-0.3. The cell suspensions were transferred to 96-well plates before spotting on agar plates, leaving every other well empty in a checkerboard manner to reduce the risk of contamination and allow more space on the agar plate for each strain. Increasing the distance between spots also strongly reduces the risk of strain interactions based on secondary metabolite production (e.g., antibiotics) that could lead to false negative results (*42*). Cell suspensions (2 µL) were spotted on top of each minimal medium plate containing individual carbon sources, as well as on a minimal medium plate without carbon source and a R-2A+M plate. Spotting was carried out using a Rainin Liquidator Manual Pipetting System (Mettler Toledo). Plates were dried under laminar flow. Bacteria were incubated at 22 °C and photographs were taken at 5, 7, and 10 days after spotting. In sum, the screen comprised three total rounds including 96 strains each, and the last round also comprised 56 randomly selected strains that were screened a second time for validation purposes (Table S7). Plate images are available through Zenodo (*82*).

Analysis of bacterial growth in carbon source screen

Colony growth was scored for all strains after 7 days (0 = no growth, 1 = growth) by comparing growth on each carbon source to the control plate without a carbon source. Here, we employed a dual approach incorporating automated growth scoring based on pixel intensities using a common threshold for all strains and manual scoring through visual inspection.

For the automated analysis, we developed the software tool 'platescan' (github.com/MicrobiologyETHZ/platescan), which enables unbiased scoring of all strains over different conditions with a firm growth cutoff. Briefly, platescan uses cross-correlation techniques to crop the plate image, locate the colony grid layout and then determine the best fitting colony size and location based on the assumption that they are approximately circular. The pixel intensities are rescaled between 1% and 99% of the intensity distribution to ensure that the images have approximately the same contrast. The program then reports foreground and background pixel intensities in red, green, blue and grayscale, which are then used to threshold growth vs. no growth. An example can be found on the program's GitHub repository.

We used platescan to assign growth values to each strain using the following parameters: -r:20, -p: 10, --min_r: 15, --max_r: 40, --edge: 200 40 200 40. In addition, two parameters were set individually for each screening round due to variation in picture zoom level. Screen1: -x 105 -y 108, screen2: -x 110 -y 109, screen3: -x 114 -y 113. We used the pixel intensities reported in the red channel with a defined minimum threshold to consider a strain as having grown. Pixel intensities were obtained by subtracting background values from foreground values for each colony and subsequently subtracting the no carbon control value. For the few cases in which strains spread into the area used for background intensity calculation, the background value of the neighboring colony was subtracted.

For a fraction of strains, we also observed substantial growth without the addition of a carbon source to the medium, suggesting that these strains could either grow on a component or impurity within the agar or were able to grow on volatile compounds present in the surrounding environment. Therefore, we also manually scored growth for all strains relative to the control plate containing no carbon. Since the magnitude of colony formation differed between carbon sources, assigning a binary growth (1) or no growth (0) value was challenging for strains that exhibited residual growth on the no carbon control or were generally slow growing. We therefore introduced a third category of non-significant (NS) growth for the initial screen analysis but considered them as no growth for subsequent analyses to keep the number of false positives low (Fig. S11A).

The results of the computational analysis using platescan and the manual analysis showed a very high overlap between the two methods. The highest overlap (with 94.6% of matches compared to the manually scored data) was obtained with a cut-off of 20 arbitrary units (a.u.).

The comparison of the manually- and computationally scored data showed that the computational method scored growth more often than the manual analysis ($n = 485$), but most of these were scored as NS initially ($n = 332$) (Fig. S12). To achieve the best accuracy possible, we applied a rigorous curation process to the screening data. First, we reinspected all cases that did not agree between the manual and computational analysis (20 a.u. cut-off) and all cases that were scored as non-significant manually. This revealed few false positive and negative scores for both the manual and computational analysis. In case of the computational analysis, these mistakes were either due to a slight misalignment of the grid or reflections on the plate. To account for slow growing strains and strains that exhibited high background growth on the no carbon control condition, we also reinspected all instances that were close to the chosen pixel cutoff (10-40 a.u.). For these, we also inspected the growth after 10 days and scored growth based on whether there was an increase in colony density over time. This latter step reduced the number of non-significant values observed in the initial analysis and mainly improved scoring of the previously mentioned slow growing Actinobacteria (Fig. S11B). The curation procedure reduced the false positive rate compared to the original analysis from 3.3% to 2.3%, while the false negative rate increased from 5.8% to 6.5%, with most uncertainty remaining for *Methylobacterium* spp. and some members of the Actinobacteria.

Plant cultivation

Plants were cultivated as described previously (*19*). In brief, *Arabidopsis thaliana* Columbia (Col-0) seeds were surface sterilized (*84*) and stratified for 4 days at 4°C. *Arabidopsis* were cultivated in six-well tissue culture plates (TechnoPlasticProducts) filled with 5 mL washed and heat sterilized calcined clay mixed with 2.5 mL half strength Murashige & Skoog medium pH 5.8 including vitamins (½ MS, Duchefa). Seeds were placed in the center of each well. If a seedling did not germinate, a seedling was transplanted from a separate plate after 7 days. Starting at day 7, each well was supplemented twice per week with 200 µL ½ MS respectively. Plates were incubated in a growth chamber (Percival, CU41-L4) set to 22°C and 54% relative humidity with a 11 h photoperiod, fitted with full spectrum lights (Philips Master TL-D 18 W/950 Graphica) and lights emitting a higher fraction of UVA and UVB (Sylvania Reptistar F18W/6500 K). The combined light intensity was set to 200-210 µmol m^{-2} s^{-1} for wavelength 400-700 nm and 4-5 µmol m^{-2} s^{-1} for wavelength 280-400 nm.

Phyllosphere inoculation

Bacteria grown on R-2A+M agar plates were suspended in 10 mM $MgCl_2$ solution and the OD_{600} was adjusted to 0.2 for each strain. The final inoculation suspension had an OD_{600} of 0.02 for all treatments. For single strain inoculations, 150 µL of OD-adjusted strain suspension was added to 1.35 mL 10 mM $MgCl_2$ solution. For two- and three-strain combinations, 75 or 50 µL of each strain were added, respectively. For the seven-strain community, 100 µL of each OD-adjusted strain suspension was mixed and then a ten-fold dilution was prepared for the final inoculum. The final suspension was mixed well and then 10 day-old *Arabidopsis* seedlings were inoculated by slowly pipetting 50 µL over the whole seedling. A ten-fold dilution series was prepared of each inoculum and spotted on R-2A+M agar plates to enumerate total bacterial load. For strain mixes appropriate dilutions were plated on R-2A+M agar plates to verify presence of all strains based on colony morphology.

Phyllosphere harvest and bacterial CFU enumeration

Bacterial colonization in the phyllosphere was enumerated when plants were 28 or 29 days old. The whole phyllosphere was harvested with sterile tweezers and a scalpel, and was placed in a 2 mL tube containing 200 µL 100 mM phosphate buffer pH 7 and a sterile 5 mm metal ball. The weight of the tube was recorded with and without the plant for plant fresh weight calculation. The harvested phyllosphere was subsequently crushed for 45 s at 30 Hz with a TissueLyser II (Qiagen). Phosphate buffer (600 µL) was added to the crushed plant material and was mixed thoroughly, 100 µL of this suspension were transferred to a 96-well plate to prepare a 10-fold dilution series in 100 mM phosphate buffer. The dilution series was spotted on R-2A+M agar plates. In addition, 50 µL of each 10^{-3} and 10^{-4}-fold dilutions were plated on 9 cm round R-2A+M agar plates. If selective plates containing streptomycin were used (for *Sphingomonas* selection), 50 µL of dilutions 10^{-1} and 10^{-2} were plated in addition. Plates were incubated at room temperature and CFU were counted after 1-3 days on dilution series and after 4-7 days on round plates. If a strain was not found on the lowest available dilution, its value was set to 0.9 CFU for this sample for further analysis. *Rhodococcus* sp. Leaf233 was selectively grown on minimal medium supplemented with maltose (5 mM) when combined with *Pseudomonas* sp. Leaf15. Colonies of Leaf233 in mixtures with *Microbacterium* sp. Leaf179 were differentiated by re-streaking colonies on minimal medium containing isoleucine. Mock treated plants ($n = 12$) were included in each plant experiment to detect any systematic contamination with external bacteria.

Shake flask cultivations

At-LSPHERE isolates grown on R-2A+M medium were suspended in 4 mL 10 mM magnesium chloride solution at an approximate OD_{600} of 3. Each strain was inoculated at an OD_{600} of 0.025 into 100 mL baffled Erlenmeyer flasks containing 10 mL of a liquid minimal medium with the same base composition (ions and vitamins) as in the carbon source screen. This medium contained all 44 growth yielding carbon sources used in the in vitro screen (Table S1) at a total concentration of 10 mM C, with each carbon source at a relative concentration corresponding to the medium composition used in the modeling. Strains were inoculated in four biological replicates in monocultures and in the pairwise and community combinations used in the plant experiments. Cultures were grown at 22˚C with shaking at 200 rpm for 60 h to allow strains to reach stationary phase. Cell numbers in each culture were enumerated via a 10-fold dilution series spotted on R-2A+M agar plates.

Data analysis

Carbon source utilization data, plant colonization experiments, and shake flask experiments were analyzed with R 4.04 in RStudio. For the carbon source screen, false positive and false negative rates were calculated based on 56 isolates that were screened twice (Table S7). The strain phylogeny was based on full length 16S rDNA gene sequences extracted from the genome sequence of each strain as described previously (*18*). Strains that did not grow on any carbon source were excluded from all further analyses. The Manhattan distances of all strains based on carbon source utilization were calculated with the *vegdist* function of the vegan 2.5 package (*95*). Hierarchical clustering was conducted with the *hclust* function with Ward method (*ward.D2*). Principal coordinate analysis was performed with the *cmdscale* function in MATLAB R2021a. Bacterial colonization data was log10 transformed to calculate the median colonization and statistical significance based on Wilcoxon rank sum test. P-values were corrected for multiple testing with the Holm method. Effect sizes for the shake flask experiments were calculated using

the *cohens_d* function (var.equal = FALSE, hedges.correction = TRUE) in the *rstatix* package (*96*). Log2 fold changes (combination/mono association) were calculated based on the median absolute abundance.

Data was visualized in R with the package ggplot2 (*97*) and was further annotated with Adobe Illustrator. For data analysis and visualization, the following R packages were used: tidyverse (*98*), ape 5.4-1 (*99*), ggridges 0.5.3 (*100*), shades1.4 (*101*), phylloR (*18*), and dendextend 1.14 (*102*).

Generation and curation of genome-scale models

We first used the tool CarveMe (*58*) to generate draft metabolic models based on the assembled genomes of each strain in the *At*-LSPHERE collection ((*53*), BioProjects PRJNA297956 and PRJEB47672). The quality of these genomes was assessed using the tool CheckM (*85*), (Table S8), which reported a mean completeness of 0.993 ± 0.007 and a mean contamination of 0.005 ± 0.007 (mean ± s.d., [0,1]). We then compared the predicted growth capabilities of each draft model against data from our in vitro carbon source screen, and performed the following steps on each draft model: first, we used the tool NICEgame ((*62*), github.com/EPFL-LCSB/NICEgame) to generate sets of new biosynthetic and transport reactions (drawn from the BiGG database (*86*)) that would allow the model to produce biomass from each growth-supporting carbon source identified in our in vitro screen. We used this process, which relies on known reaction thermodynamic constraints (*87*, *88*), to produce at most five alternative sets of reactions for each growth-supporting carbon source. We separately integrated each set of reactions into the draft model and tested whether or not it could produce biomass on a simulated minimal medium (Table S6) supplemented with each of the 45 carbon sources used in the in vitro screen. We also tested the growth of the model when combinations of reaction sets from up to three carbon sources were integrated, selecting the most accurate model (i.e., the most representative with the fewest false positives) as measured by Matthews Correlation Coefficient $((TP \times TN - FP \times FN)/\sqrt{(TP + FP)(TP + FN)(TN + FP)(TN + FN)})$ for further curation. Most models reached this stage having had sets of reactions from only one (111 models) or two (82 models) growth-supporting carbon sources integrated, as adding reactions that enable growth on one resource can resolve additional gaps that enable growth on other resources. The carbon sources most often used for gap-filling were maltose, succinate, gluconate, and xylose (being used to gap-fill 40, 26, 23, and 21 models, respectively). To correct for remaining false negatives (i.e., the model did not grow on a carbon source that supported growth in vitro), we further added reactions from a different model in our collection that did recapitulate growth on the relevant carbon source. A maximum false positive rate of either 10 carbon sources or half of all true positives for the model, whichever was smaller, was set to avoid integrating an excessive number of new reactions. False positives for a given carbon source were corrected by removing internal reactions relevant to its metabolism, or by restricting the relevant transport reaction when this was not successful. Model- and carbon source-specific accuracies are summarized in Fig. S5, and reactions added to the models as part of the curation are enumerated in Fig. S4 and Table S3. We identified no relationship between model accuracy and either the size (Fig. S6B) or the completeness of the underlying genome (Figure S13). A final quality control was performed on each model (*59*), consisting of testing for mass and charge balance, performing a leak test to ensure no metabolites could be produced from nothing, standardizing the metabolite namespace, adding reaction subsystems, and adding additional gene, metabolite, and reaction identifiers when available. A final report was generated for each model using the validation tool MEMOTE (total score = 0.84 ± 0.02 (mean ± s.d., $n = 224$)) (*89*), and balanced accuracies for individual

models and pairwise interaction predictions were calculated as $(TPR + TNR)/2$, where TPR and TNR represent the true positive rate and false positive rates, respectively. All scripts for model generation and simulation, as well as the models and quality reports, are available at github.com/VorholtLab/i-At-LSPHERE.

Computing mono- and coculture growth

All growth simulations were performed using the COBRA Toolbox v2.24.3 (*90*) with the CPLEX solver v12.10 (IBM) in MATLAB R2021a (MathWorks). Nonlimiting amounts ($v_{max} =$ 1000 mmol/gDW/hr) of a minimal medium composition containing ions, water, and sources of nitrogen, sulfur, and phosphorus were provided to the models, along with vitamins at $v_{max} =$ 0.15 mmol/gDW/hr (Table S6). Limiting amounts of the 45 carbon sources tested in our in vitro screen were provided at abundances intended to broadly estimate the relative availabilities of resource types on leaf surfaces (*36*, *38*, *39*, *54*) ($v_{max} = 0.15$ mmol/gDW/hr for sugars and organic acids, 0.075 mmol/gDW/hr for amino acids, and 1.5 mmol/gDW/hr for methanol). Model growth was simulated with biomass as the objective function and a minimal ATP maintenance flux of 0.5 mmol/gDW/hr. Optimizations were also set to minimize all reaction fluxes to more closely simulate efficient proteome utilization and minimize metabolite cycling (*91*). For each pair or community, the growth of each strain was first simulated individually, and the resulting biomass flux values and resource uptake fluxes were recorded. Models were then merged by integrating them into a common extracellular compartment (*92*, *93*). Coupling constraints were introduced in order to avoid infeasible solutions in which one organism produced metabolic flux for the other without producing biomass itself (*34*, *94*). Additionally, metabolite uptake directionalities were fixed to those observed in monoculture to minimize inconsistencies in resource preferences between mono- and coculture. The sum of biomass reactions was set as the objective to be optimized, and exchange reaction v_{max} values were set as equal to those of the models in monoculture, thus simulating an equal abundance of resources between the mono- and coculture conditions. The resulting biomass flux values were recorded and used to calculate interaction scores, which were defined as the log2 ratio of biomass flux in coculture to that in monoculture. Interaction scores were limited to between -5 and 5, with extreme log2 fold changes falling outside this range being set to -5 or 5.

References and Notes

1. A. Apprill, Marine Animal Microbiomes: Toward understanding host–microbiome interactions in a changing ocean. *Frontiers in Marine Science*. **4**, 222 (2017).
2. E. A. Archie, J. Tung, Social behavior and the microbiome. *Current Opinion in Behavioral Sciences*. **6**, 28–34 (2015).
3. J. Lloyd-Price, A. Mahurkar, G. Rahnavard, J. Crabtree, J. Orvis, *et al.*, Strains, functions and dynamics in the expanded Human Microbiome Project. *Nature*. **550**, 61–66 (2017).
4. R. Knight, C. Callewaert, C. Marotz, E. R. Hyde, J. W. Debelius, *et al.*, The microbiome and human biology. *Annual Review of Genomics and Human Genetics*. **18**, 65–86 (2017).
5. P. Trivedi, J. E. Leach, S. G. Tringe, T. Sa, B. K. Singh, Plant–microbiome interactions: from community assembly to plant health. *Nature Reviews Microbiology*. **18**, 607–621 (2020).
6. L. S. Bittleston, M. Gralka, G. E. Leventhal, I. Mizrahi, O. X. Cordero, Context-dependent dynamics lead to the assembly of functionally distinct microbial communities. *Nature Communications*. **11**, 1440 (2020).

7. J. E. Goldford, N. Lu, D. Bajić, S. Estrela, M. Tikhonov, *et al.*, Emergent simplicity in microbial community assembly. *Science*. **361**, 469–474 (2018).

8. S. Estrela, J. C. C. Vila, N. Lu, D. Bajić, M. Rebolleda-Gómez, *et al.*, Functional attractors in microbial community assembly. *Cell Systems*. **13**, 29-42.e7 (2022).

9. V. Dubinkina, Y. Fridman, P. P. Pandey, S. Maslov, Multistability and regime shifts in microbial communities explained by competition for essential nutrients. *eLife*. **8**, e49720 (2019).

10. A. R. Pacheco, M. L. Osborne, D. Segrè, Non-additive microbial community responses to environmental complexity. *Nature Communications*. **12**, 2365 (2021).

11. J. Friedman, L. M. Higgins, J. Gore, Community structure follows simple assembly rules in microbial microcosms. *Nature Ecology & Evolution*. **1**, 0109 (2017).

12. O. S. Venturelli, A. V Carr, G. Fisher, R. H. Hsu, R. Lau, *et al.*, Deciphering microbial interactions in synthetic human gut microbiome communities. *Molecular Systems Biology*. **14**, 1–19 (2018).

13. A. L. Gould, V. Zhang, L. Lamberti, E. W. Jones, B. Obadia, *et al.*, Microbiome interactions shape host fitness. *Proceedings of the National Academy of Sciences*. **115**, E11951-E11960 (2018).

14. T. Camenzind, S. Hättenschwiler, K. K. Treseder, A. Lehmann, M. C. Rillig, Nutrient limitation of soil microbial processes in tropical forests. *Ecological Monographs*. **88**, 4–21 (2018).

15. M. E. Hibbing, C. Fuqua, M. R. Parsek, S. B. Peterson, Bacterial competition: surviving and thriving in the microbial jungle. *Nature Reviews Microbiology*. **8**, 15–25 (2010).

16. K. Vrede, M. Heldal, S. Norland, G. Bratbak, Elemental composition (C, N, P) and cell volume of exponentially growing and nutrient-limited bacterioplankton. *Applied and Environmental Microbiology*. **68**, 2965–2971 (2002).

17. J. Kehe, A. Ortiz, A. Kulesa, J. Gore, P. C. Blainey, *et al.*, Positive interactions are common among culturable bacteria. *Science Advances*. **7159**, 1–11 (2021).

18. C. I. Carlström, C. M. Field, M. Bortfeld-Miller, B. Müller, S. Sunagawa, *et al.*, Synthetic microbiota reveal priority effects and keystone strains in the Arabidopsis phyllosphere. *Nature Ecology and Evolution*. **3**, 1445–1454 (2019).

19. M. Schäfer, C. M. Vogel, M. Bortfeld-Miller, M. Mittelviefhaus, J. A. Vorholt, Mapping phyllosphere microbiota interactions in planta to establish genotype–phenotype relationships. *Nature Microbiology*. **7**, 856–867 (2022).

20. K. R. Foster, T. Bell, Competition, not cooperation, dominates interactions among culturable microbial species. *Current Biology*. **22**, 1845–1850 (2012).

21. R. Levins, *Evolution in Changing Environments* (Princeton University Press, 1968; http://www.jstor.org/stable/10.2307/j.ctvx5wbbh).

22. S. H. Hurlbert, The Measurement of Niche Overlap and Some Relatives. *Ecology*. **59**, 67–77 (1978).

23. M. Wilson, S. E. Lindow, Coexistence among epiphytic bacterial populations mediated through nutritional resource partitioning. *Applied and Environmental Microbiology*. **60**, 4468–4477 (1994).

24. S. Li, J. Tan, X. Yang, C. Ma, L. Jiang, Niche and fitness differences determine invasion success and impact in laboratory bacterial communities. *The ISME Journal*. **13**, 402–412 (2019).

25. M. Advani, G. Bunin, P. Mehta, Statistical physics of community ecology: a cavity solution to MacArthur's consumer resource model. *Journal of Statistical Mechanics: Theory and Experiment*. **2018**, 033406 (2018).

26. N. Einat, T. Gal, F. Jonathan, Interactions between culturable bacteria are predicted by individual species' growth. *mSystems*. **0**, e00836-22 (2023).

27. L. C. Birch, The meanings of competition. *The American Naturalist*. **91**, 5–18 (1957).

28. P. Chesson, Mechanisms of maintenance of species diversity. *Annual Review of Ecology and Systematics*. **31**, 343–366 (2003).

29. S. Freilich, R. Zarecki, O. Eilam, E. S. Segal, C. S. Henry, *et al.*, Competitive and cooperative metabolic interactions in bacterial communities. *Nature Communications*. **2**, 587–589 (2011).

30. M. Tikhonov, Community-level cohesion without cooperation. *eLife.* **5**, e15747 (2016).

31. J. D. Orth, I. Thiele, B. Ø. O. Palsson, What is flux balance analysis? *Nature Biotechnology*. **28**, 245–248 (2010).

32. A. Bordbar, J. M. Monk, Z. A. King, B. O. Palsson, Constraint-based models predict metabolic and associated cellular functions. *Nature Reviews Genetics*. **15**, 107–120 (2014).

33. N. Y. D. Ankrah, D. B. Bernstein, M. Biggs, M. Carey, M. Engevik, *et al.*, Enhancing microbiome research through genome-scale metabolic modeling. *mSystems*. **6**, e00599-21 (2021).

34. S. Magnúsdóttir, A. Heinken, L. Kutt, D. A. Ravcheev, E. Bauer, *et al.*, Generation of genome-scale metabolic reconstructions for 773 members of the human gut microbiota. *Nature Biotechnology.* **35**, 81-89 (2016).

35. M. Kumar, B. Ji, K. Zengler, J. Nielsen, Modelling approaches for studying the microbiome. *Nature Microbiology*. **4**, 1253–1267 (2019).

36. S. E. Lindow, M. T. Brandl, Microbiology of the phyllosphere. *Applied and Environmental Microbiology*. **69**, 1875–1883 (2003).

37. J. A. Vorholt, Microbial life in the phyllosphere. *Nature Reviews Microbiology*. **10**, 828–840 (2012).

38. J. H. J. Leveau, S. E. Lindow, Appetite of an epiphyte: Quantitative monitoring of bacterial sugar consumption in the phyllosphere. *Proceedings of the National Academy of Sciences*. **98**, 3446–3453 (2001).

39. F. Ryffel, E. J. N. Helfrich, P. Kiefer, L. Peyriga, J. C. Portais, *et al.*, Metabolic footprint of epiphytic bacteria on *Arabidopsis thaliana* leaves. *ISME Journal*. **10**, 632–643 (2016).

40. G. Innerebner, C. Knief, J. A. Vorholt, Protection of *Arabidopsis thaliana* against leaf-pathogenic *Pseudomonas syringae* by *Sphingomonas* strains in a controlled model system. *Applied and Environmental Microbiology*. **77**, 3202–3210 (2011).

41. U. Ritpitakphong, L. Falquet, A. Vimoltust, A. Berger, J. Métraux, *et al.*, The microbiome of the leaf surface of Arabidopsis protects against a fungal pathogen. *New Phytologist*. **210**, 1033–1043 (2016).

42. C. M. Vogel, D. B. Potthoff, M. Schäfer, N. Barandun, J. A. Vorholt, Protective role of the Arabidopsis leaf microbiota against a bacterial pathogen. *Nature Microbiology*. **6**, 1537–1548 (2021).

43. C. E. Morris, L. L. Kinkel, "Fifty years of phyllosphere microbiology: significant contributions to research in related fields" in *Phyllosphere Microbiology*, S. E. Lindow, E. I. Hecht-Poinar, V. J. Elliott, Eds. (APS Press, St. Paul, Minnesota, Minnesota, 2002), pp. 365–375.

44. J. Peñuelas, J. Terradas, The foliar microbiome. *Trends in Plant Science*. **19**, 278–280 (2014).

45. B. K. Singh, P. Trivedi, E. Egidi, C. A. Macdonald, M. Delgado-Baquerizo, Crop microbiome and sustainable agriculture. *Nature Reviews Microbiology*. **18**, 601–602 (2020).

46. F. Martinelli, R. Scalenghe, S. Davino, S. Panno, G. Scuderi, *et al.*, Advanced methods of plant disease detection. A review. *Agronomy for Sustainable Development*. **35**, 1–25 (2015).

47. A. R. Pacheco, J. A. Vorholt, Resolving metabolic interaction mechanisms in plant microbiomes. *Current Opinion in Microbiology*. **74**, 102317 (2023).

48. A. M. Geller, A. Levy, "What I cannot create, I do not understand": elucidating microbe–microbe interactions to facilitate plant microbiome engineering. *Current Opinion in Microbiology*. **72**, 102283 (2023).

49. J. A. Vorholt, C. Vogel, C. I. Carlström, D. B. Müller, Establishing Causality: Opportunities of synthetic communities for plant microbiome research. *Cell Host and Microbe*. **22**, 142–155 (2017).

50. A. S. Weiss, A. G. Burrichter, A. C. Durai Raj, A. von Strempel, C. Meng, *et al.*, In vitro interaction network of a synthetic gut bacterial community. *The ISME Journal*. **16**, 1095–1109 (2022).

51. J. J. Faith, P. P. Ahern, V. K. Ridaura, J. Cheng, J. I. Gordon, Identifying gut microbe–host phenotype relationships using combinatorial communities in gnotobiotic mice. *Science Translational Medicine*. **6**, 220ra11 (2014).

52. J. Coker, K. Zhalnina, C. Marotz, D. Thiruppathy, M. Tjuanta, *et al.*, A reproducible and tunable synthetic soil microbial community provides new insights into microbial ecology. *mSystems*. **7**, e00951-22 (2022).

53. Y. Bai, D. B. Müller, G. Srinivas, R. Garrido-Oter, E. Potthoff, *et al.*, Functional overlap of the Arabidopsis leaf and root microbiota. *Nature*. **528**, 364–369 (2015).

54. H. B. Tukey, The leaching of substances from plants. *Annual Review of Plant Physiology*. **21**, 305–324 (1970).

55. M. J. Poupin, T. Ledger, R. Roselló-Móra, B. González, The Arabidopsis holobiont: a (re)source of insights to understand the amazing world of plant–microbe interactions. *Environmental Microbiome*. **18**, 9 (2023).

56. P. Vaz Jauri, L. L. Kinkel, Nutrient overlap, genetic relatedness and spatial origin influence interaction-mediated shifts in inhibitory phenotype among Streptomyces spp. *FEMS Microbiology Ecology*. **90**, 264–275 (2014).

57. M. Michalska-Smith, Z. Song, S. A. Spawn-Lee, Z. A. Hansen, M. Johnson, *et al.*, Network structure of resource use and niche overlap within the endophytic microbiome. *The ISME Journal*. **16**, 1–12 (2021).

58. D. Machado, S. Andrejev, M. Tramontano, K. R. Patil, Fast automated reconstruction of genome-scale metabolic models for microbial species and communities. *Nucleic Acids Research*. **46**, 7542–7553 (2018).

59. I. Thiele, B. O. Palsson, A protocol for generating a high-quality genome-scale metabolic reconstruction. *Nature Protocols*. **5**, 93-121 (2010).

60. S. N. Mendoza, B. G. Olivier, D. Molenaar, B. Teusink, A systematic assessment of current genome-scale metabolic reconstruction tools. *Genome Biology*. **20**, 158 (2019).

61. D. B. Bernstein, S. Sulheim, E. Almaas, D. Segrè, Addressing uncertainty in genome-scale metabolic model reconstruction and analysis. *Genome Biology 2021 22:1*. **22**, 1–22 (2021).

62. E. Vayena, A. Chiappino-Pepe, H. MohammadiPeyhani, Y. Francioli, N. Hadadi, *et al.*, A workflow for annotating the knowledge gaps in metabolic reconstructions using known and hypothetical reactions. *Proceedings of the National Academy of Sciences*. **119**, e2211197119 (2022).

63. J. A. Valderrama, G. Durante-Rodríguez, B. Blázquez, J. L. García, M. Carmona, *et al.*, Bacterial degradation of benzoate: cross-regulation between aerobic and anaerobic pathways. *The Journal of Biological Chemistry*. **287**, 10494–10508 (2012).

64. G. Fuchs, M. Boll, J. Heider, Microbial degradation of aromatic compounds — from one strategy to four. *Nature Reviews Microbiology*. **9**, 803–816 (2011).

65. M. Murillo-Roos, H. S. M. Abdullah, M. Debbar, N. Ueberschaar, M. T. Agler, Cross-feeding niches among commensal leaf bacteria are shaped by the interaction of strain-level diversity and resource availability. *The ISME Journal*. **16**, 2280–2289 (2022).

66. B. Ryback, M. Bortfeld-Miller, J. A. Vorholt, Metabolic adaptation to vitamin auxotrophy by leaf-associated bacteria. *The ISME Journal*. **16**, 2712–2724 (2022).

67. L. Hemmerle, B. A. Maier, M. Bortfeld-Miller, B. Ryback, C. G. Gäbelein, *et al.*, Dynamic character displacement among a pair of bacterial phyllosphere commensals in situ. *Nature Communications*. **13**, 2836 (2022).

68. A. P. Goldberg, B. Szigeti, Y. H. Chew, J. A. Sekar, Y. D. Roth, *et al.*, Emerging whole-cell modeling principles and methods. *Current Opinion in Biotechnology*. **51**, 97–102 (2018).

69. D. B. Bernstein, B. Akkas, M. N. Price, A. P. Arkin, Critical assessment of E. coli genome-scale metabolic model with high-throughput mutant fitness data. *bioRxiv* (2023), doi:10.1101/2023.01.05.522875.

70. C. M. J. Pieterse, C. Zamioudis, R. L. Berendsen, D. M. Weller, S. C. M. Van Wees, *et al.*, Induced systemic resistance by beneficial microbes. *Annual review of phytopathology*. **52**, 347–75 (2014).

71. K. Wang, A. Auzane, K. Overmyer, The immunity priming effect of the Arabidopsis phyllosphere resident yeast *Protomyces arabidopsidicola* strain C29. *Frontiers in Microbiology*. **13**, 956018 (2022).

72. E. J. N. Helfrich, C. M. Vogel, R. Ueoka, M. Schäfer, F. Ryffel, *et al.*, Bipartite interactions, antibiotic production and biosynthetic potential of the Arabidopsis leaf microbiome. *Nature Microbiology*. **3**, 909–919 (2018).

73. B. A. Maier, P. Kiefer, C. M. Field, L. Hemmerle, M. Bortfeld-Miller, *et al.*, A general non-self response as part of plant immunity. *Nature Plants*. **7**, 696–705 (2021).

74. R. O. Schlechter, M. Miebach, M. N. P. Remus-Emsermann, Driving factors of epiphytic bacterial communities: A review. *Journal of Advanced Research*. **19**, 57–65 (2019).

75. T. Orevi, N. Kashtan, Life in a droplet: Microbial ecology in microscopic surface wetness. *Frontiers in Microbiology*. **12**, 655459 (2021).

76. J. A. Cole, L. Kohler, J. Hedhli, Z. Luthey-Schulten, Spatially-resolved metabolic cooperativity within dense bacterial colonies. *BMC Systems Biology*. **9**, 15 (2015).

77. E. Bauer, J. Zimmermann, F. Baldini, I. Thiele, C. Kaleta, BacArena: Individual-based metabolic modeling of heterogeneous microbes in complex communities. *PLOS Computational Biology*. **13**, e1005544 (2017).

78. I. Dukovski, D. Bajić, J. M. Chacón, M. Quintin, J. C. C. Vila, *et al.*, A metabolic modeling platform for the computation of microbial ecosystems in time and space (COMETS). *Nature Protocols*. **16**, 5030–5082 (2021).

79. L. Angeles-Martinez, V. Hatzimanikatis, Spatio-temporal modeling of the crowding conditions and metabolic variability in microbial communities. *PLOS Computational Biology*. **17**, e1009140 (2021).

80. A. R. Pacheco, VorholtLab/i-At-LSPHERE: v1.0 (2023), doi:10.5281/zenodo.7915630.

81. C. M. Field, MicrobiologyETHZ/platescan: v1.0 (2023), doi:10.5281/zenodo.7898736.

82. M. Schäfer, Images of colony growth for 224 *Arabidopsis thaliana* bacterial strains on 46 carbon sources (2023), doi:10.5281/zenodo.7915606.

83. R. Peyraud, P. Kiefer, P. Christen, S. Massou, J.-C. Portais, *et al.*, Demonstration of the ethylmalonyl-CoA pathway by using 13 C metabolomics. *Proceedings of the National Academy of Sciences*. **106**, 4846–4851 (2009).

84. B. Schlesier, F. Bréton, H.-P. Mock, A hydroponic culture system for growing *Arabidopsis thaliana* plantlets under sterile conditions. *Plant Molecular Biology Reporter*. **21**, 449–456 (2003).

85. D. H. Parks, M. Imelfort, C. T. Skennerton, P. Hugenholtz, G. W. Tyson, CheckM: assessing the quality of microbial genomes recovered from isolates, single cells, and metagenomes. *Genome Research*. **25**, 1043–1055 (2015).

86. Z. A. King, J. Lu, A. Dräger, P. Miller, S. Federowicz, *et al.*, BiGG Models: A platform for integrating, standardizing and sharing genome-scale models. *Nucleic Acids Research*. **44**, D515–D522 (2016).

87. C. S. Henry, L. J. Broadbelt, V. Hatzimanikatis, Thermodynamics-based metabolic flux analysis. *Biophysical Journal*. **92**, 1792–1805 (2007).

88. P. Salvy, G. Fengos, M. Ataman, T. Pathier, K. C. Soh, *et al.*, pyTFA and matTFA: a Python package and a Matlab toolbox for thermodynamics-based flux analysis. *Bioinformatics.* **35**, 167-169 (2018).

89. C. Lieven, M. E. Beber, B. G. Olivier, F. T. Bergmann, M. Ataman, *et al.*, MEMOTE for standardized genome-scale metabolic model testing. *Nature Biotechnology*. **38**, 272–276 (2020).

90. L. Heirendt, S. Arreckx, T. Pfau, S. N. Mendoza, A. Richelle, *et al.*, Creation and analysis of biochemical constraint-based models using the COBRA Toolbox v.3.0. *Nature Protocols*. **14**, 639–702 (2019).

91. N. E. Lewis, K. K. Hixson, T. M. Conrad, J. A. Lerman, P. Charusanti, *et al.*, Omic data from evolved *E. coli* are consistent with computed optimal growth from genome-scale models. *Molecular Systems Biology*. **6**, 390 (2010).

92. N. Klitgord, D. Segrè, Environments that induce synthetic microbial ecosystems. *PLoS Computational Biology*. **6**, e1001002 (2010).

93. A. Heinken, I. Thiele, Anoxic conditions promote species-specific mutualism between gut microbes in silico. *Applied and Environmental Microbiology*. **81**, 4049–4061 (2015).

94. A. Heinken, S. Sahoo, R. M. T. Fleming, I. Thiele, Systems-level characterization of a host-microbe metabolic symbiosis in the mammalian gut. *Gut Microbes*. **4**, 28-40 (2013).

95. J. Oksanen, G. L. Simpson, F. G. Blanchet, R. Kindt, P. Legendre, *et al.*, vegan: Community Ecology Package. **v. 2.5-7** (2020) (available at https://cran.r-project.org/package=vegan).

96. A. Kassambara, rstatix: Pipe-Friendly Framework for Basic Statistical Tests. **v.0.7.2** (2023) (available at cran.r-project.org/web/packages/rstatix).

97. H. Wickham, ggplot2: Elegant Graphics for Data Analysis. *Springer-Verlag New York* (2016) (available at https://ggplot2.tidyverse.org).

98. H. Wickham, M. Averick, J. Bryan, W. Chang, L. McGowan, *et al.*, Welcome to the Tidyverse. *Journal of Open Source Software*. **4**, 1686 (2019).

99. E. Paradis, K. Schliep, ape 5.0: an environment for modern phylogenetics and evolutionary analyses in R. *Bioinformatics*. **35**, 526–528 (2019).

100. C. O. Wilke, ggridges: Ridgeline Plots in "ggplot2" (2022).

101. J. Clayden, shades: Simple Colour Manipulation (2019).

102. T. Galili, dendextend: an R package for visualizing, adjusting and comparing trees of hierarchical clustering. *Bioinformatics*. **31**, 3718–3720 (2015).

Acknowledgments: We thank Salome Hegi and Michael Berger for experimental support, Aslı Şahin, Omid Oftadeh, and Daniel Machado for helpful discussions on the metabolic modeling, and Christine Pestalozzi for contributing to the visualization shown in Fig. 3B.

Funding:

Swiss National Science Foundation grant NRP72 (JAV)

European Research Council Advanced Grant (PhyMo; no. 668991) (JAV)

Swiss National Science Foundation grant 200021_188623 (VH)

NCCR Microbiomes, Swiss National Science Foundation (51NF40_180575) (VH, JAV)

James S. McDonnell Postdoctoral Fellowship (2020-1332) (ARP)

Author contributions:

Conceptualization: MS, ARP, JAV

Methodology: MS, ARP, CMF, EV, VH

Investigation: MS, ARP, RK, MBM

Visualization: MS, ARP

Funding acquisition: ARP, VH, JAV

Project administration: JAV

Supervision: VH, JAV

Writing – original draft: MS, ARP, JAV

Writing – review & editing: MS, ARP, RK, MBM, EV, CMF, VH, JAV

Competing interests: Authors declare that they have no competing interests.

Data and materials availability: Materials and methods are available as supplementary materials. The collection of genome-scale models, as well as scripts for generating the models and conducting simulations are available through Zenodo (*80*). The platescan software (*81*) and plate images used for the carbon source screen (*82*) are available through Zenodo.

Figures

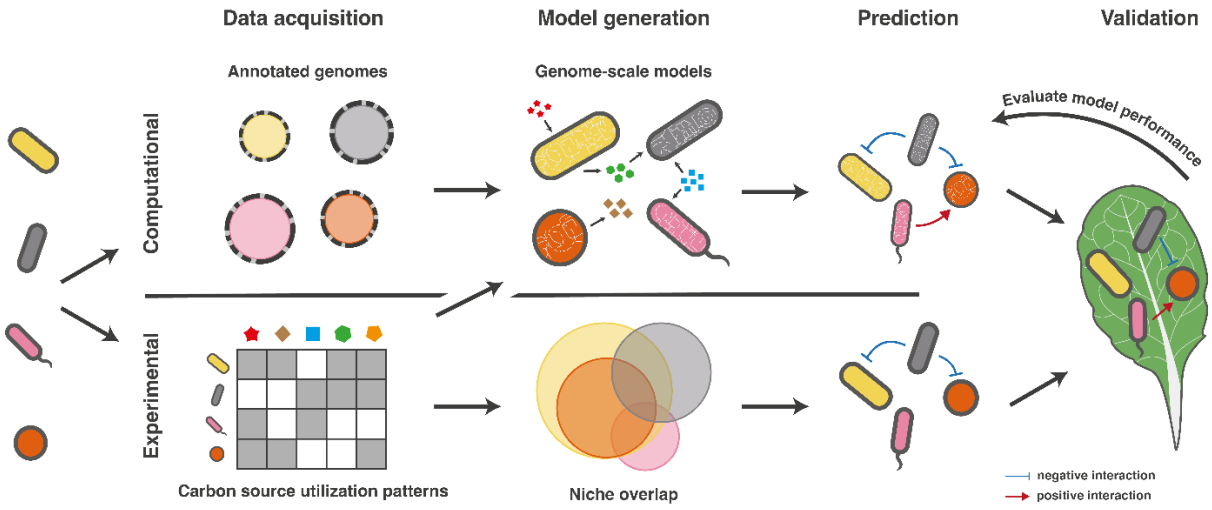

Fig. 1.
Overview of experimentally- and computationally-guided prediction and testing of metabolic interactions among bacterial members of the *Arabidopsis* phyllosphere microbiota.

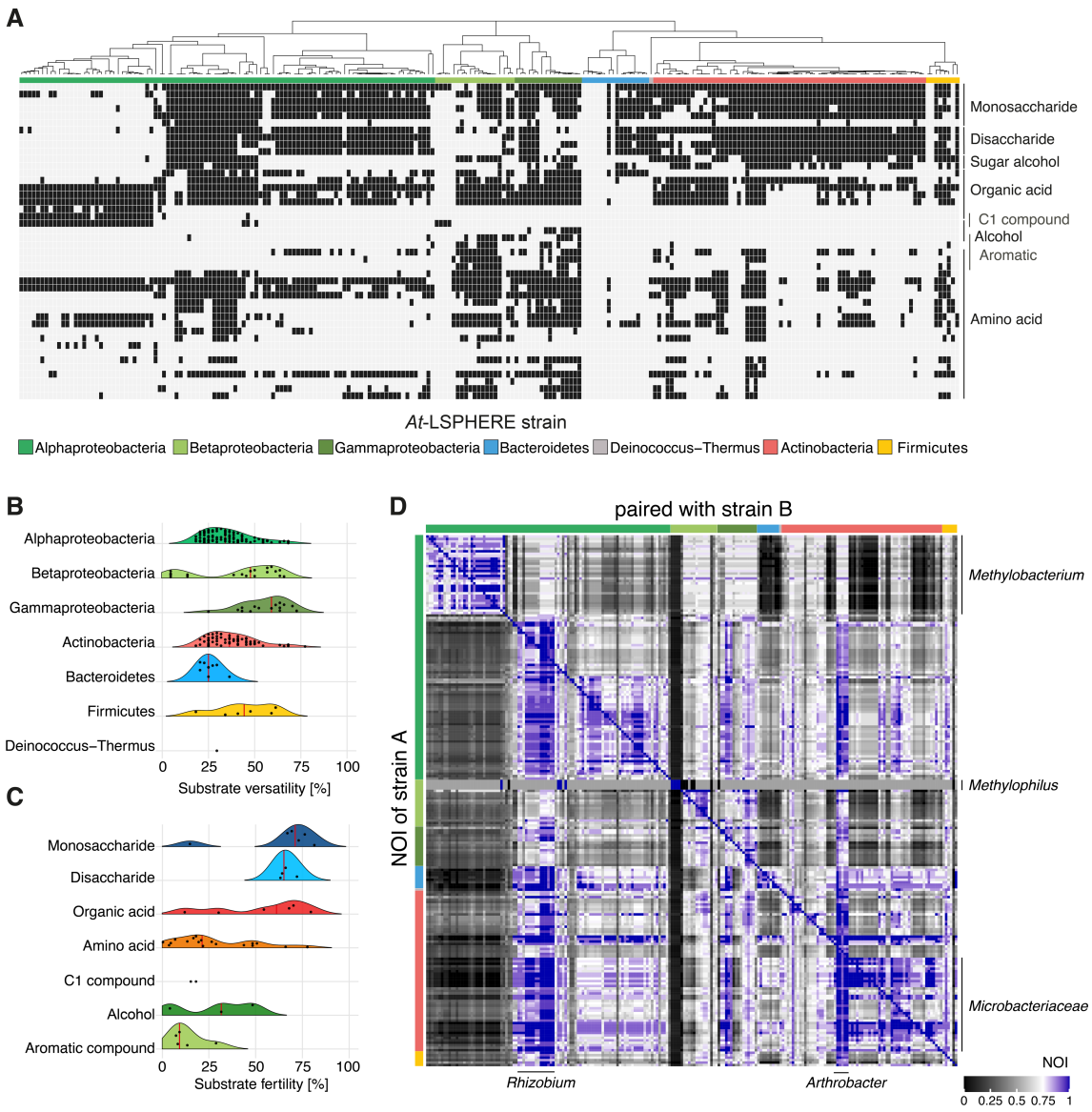

Fig. 2.

Carbon source utilization screen reveals hotspots of high nutritional niche overlap. **A)** Carbon source utilization map of 224 *At*-LSPHERE strains. Fill color of the boxes indicate growth (black) or no growth (grey) for each strain on the x-axis on a given carbon source on the y-axis. Top-level clustering for strains reflects phylogeny based on full length 16S rRNA gene sequences. Colored bars indicate phylum or Proteobacterium class and correspond to the order in the legend. Carbon sources are sorted by compound groups**. B, C)** Density plots showing (B) strain-specific versatility grouped by phylum or Proteobacterium class (corresponding to the order in the legend) and (C) substrate fertility grouped by compound group. Black dots indicate individual values, and the red vertical line shows the median for each group. Substrates in classes C1 and aromatic compounds that also fall into another substrate group are only shown once and omitted from the other. **D)** Heatmap of niche overlap indices (NOI) for all binary combinations of 215 *At*-LSPHERE strains. The color of the tile indicates high (> 0.75, blue shades) or low (< 0.75, grey shades) degree of niche overlap for the strain on the y-axis in combination with the strain on the x-axis. Strains are sorted by phylogeny and the colored bars indicate the phylum or Proteobacterium class. NOI was only calculated for strains that grew on ≥1 C-source in vitro.

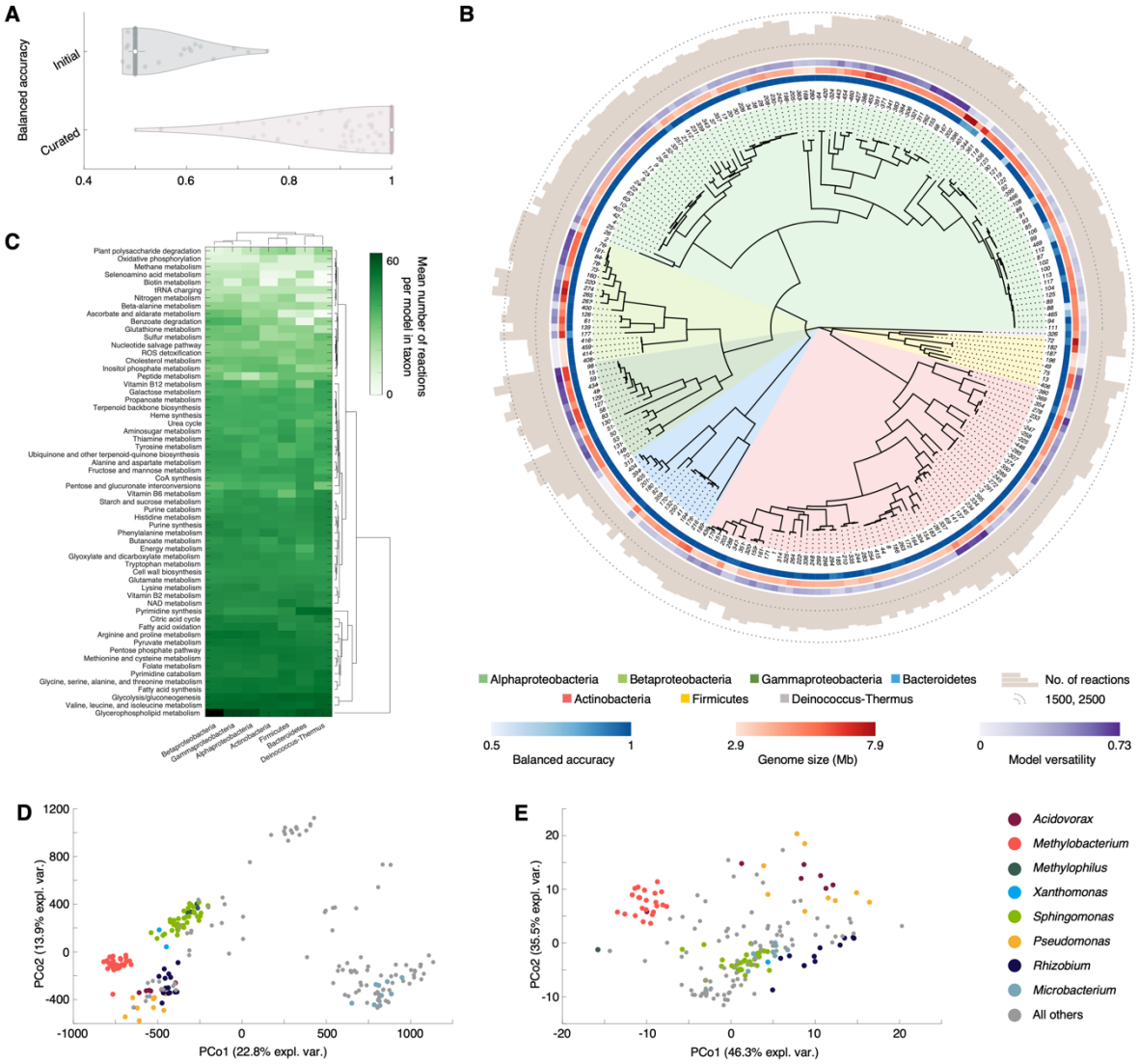

Fig. 3.

Overview of collection of metabolic models for 224 bacterial members of the *Arabidopsis thaliana* leaf microbiota. **A)** Distributions of balanced accuracy as tested on 45 carbon sources for models generated solely from genomic information (top) and after curation (bottom). **B)** Attributes of models as clustered by taxonomic phylum/class. Numbers bordering phylogenetic tree denote strain identity (e.g., 220 corresponds to *Xylophilus* sp. Leaf220). Innermost ring represents the balanced accuracy of each model, second ring indicates the size of the genome used to generate each model (*53*), and third ring represents the versatility *V* of each model. Outermost bars represent the number of reactions contained in each model (min = 1,568, max = 3,004). **C)** Clustered heatmap of 60 most highly represented reaction types, scaled by the number of models corresponding to each phylum/class. **D, E)** Principal coordinates analysis of strains as determined by (D) reactions in genome-scale models and (E) in vitro carbon source screen, with select genera highlighted.

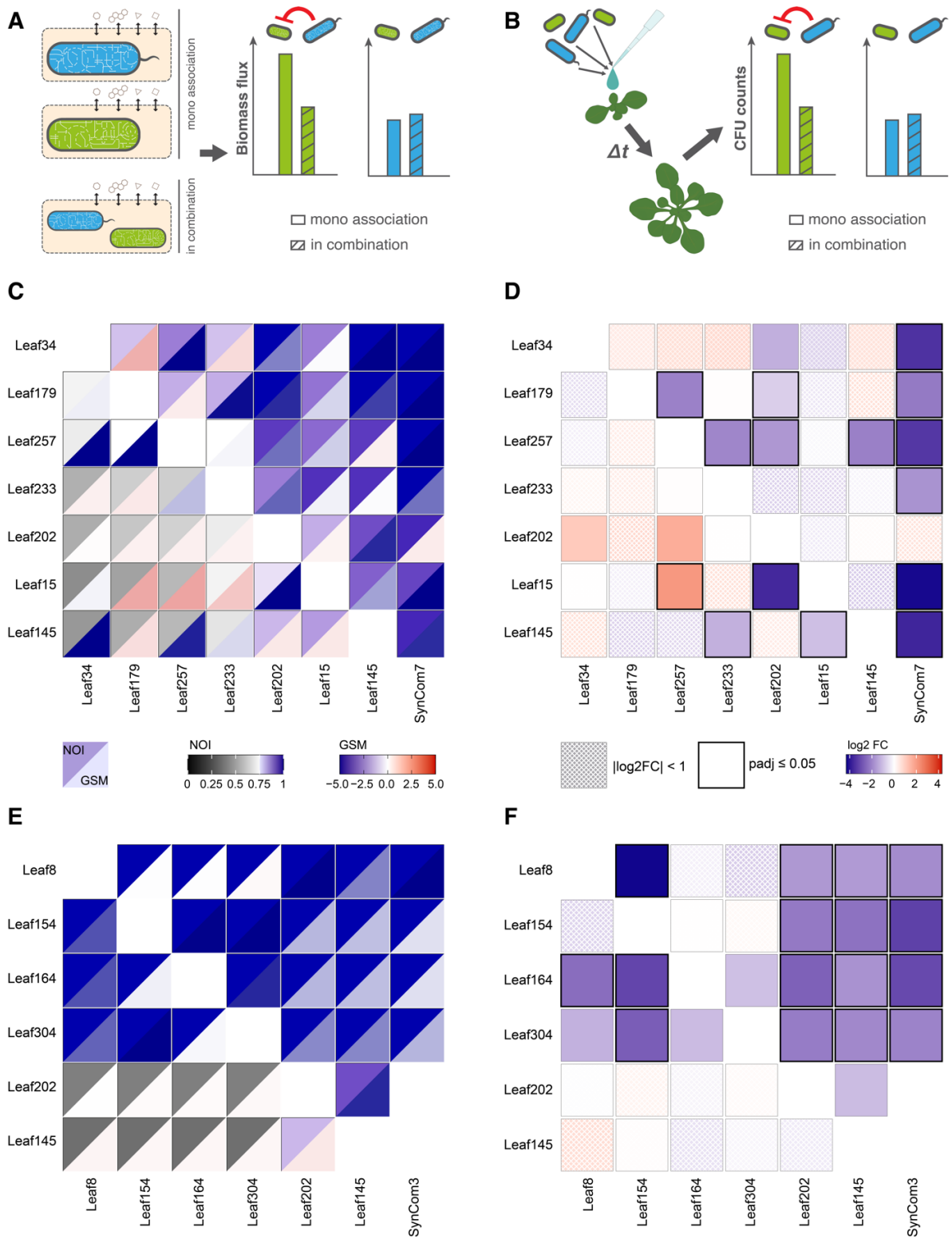

Fig. 4.

Model predictions and in planta validation of interactions. **A, B)** Schematic overview of interaction simulations using genome-scale models (A) and of phyllosphere inoculation and interaction mapping procedure (B). Interactions are inferred by comparing a strain's growth in combination with another strain with that in monoculture. This is computed as the log2 ratio of

biomass fluxes for the genome-scale models or as the log2 fold change in CFUs per gram plant fresh weight for the in planta experiments. **C, E)** Predicted interaction outcome for the strain indicated on the y-axis in combination with the strain or SynCom indicated on the x-axis based on niche overlap index (NOI, top left) and genome scale models (GSM, bottom right). The fill color indicates high (> 0.75, blue shades) or low (< 0.75, grey shades) degree of niche overlap and predicted positive (red shades) or negative (blue shades) interactions based on genome scale metabolic models. **D, F)** Interaction outcomes observed in planta. Heatmap showing the log_2FCs (pairwise/SynCom inoculation vs mono-association) for the strain on the y-axis in combination with the strain or SynCom indicated on the x-axis based on absolute abundances obtained by CFU enumeration (n =11-12). The color of the boxes reflects the observed log_2FC and the black frames around the boxes indicate a significant difference compared with the mono-association condition (two-sided Wilcoxon rank-sum test, Holm adjusted $P \leq 0.05$). |Log2FC| < 1 are overlaid with a crosshatched pattern. Confusion matrices comparing modeling predictions and in planta outcomes are provided in Table S4, and colony counts for the in planta experiments are provided in Table S5.

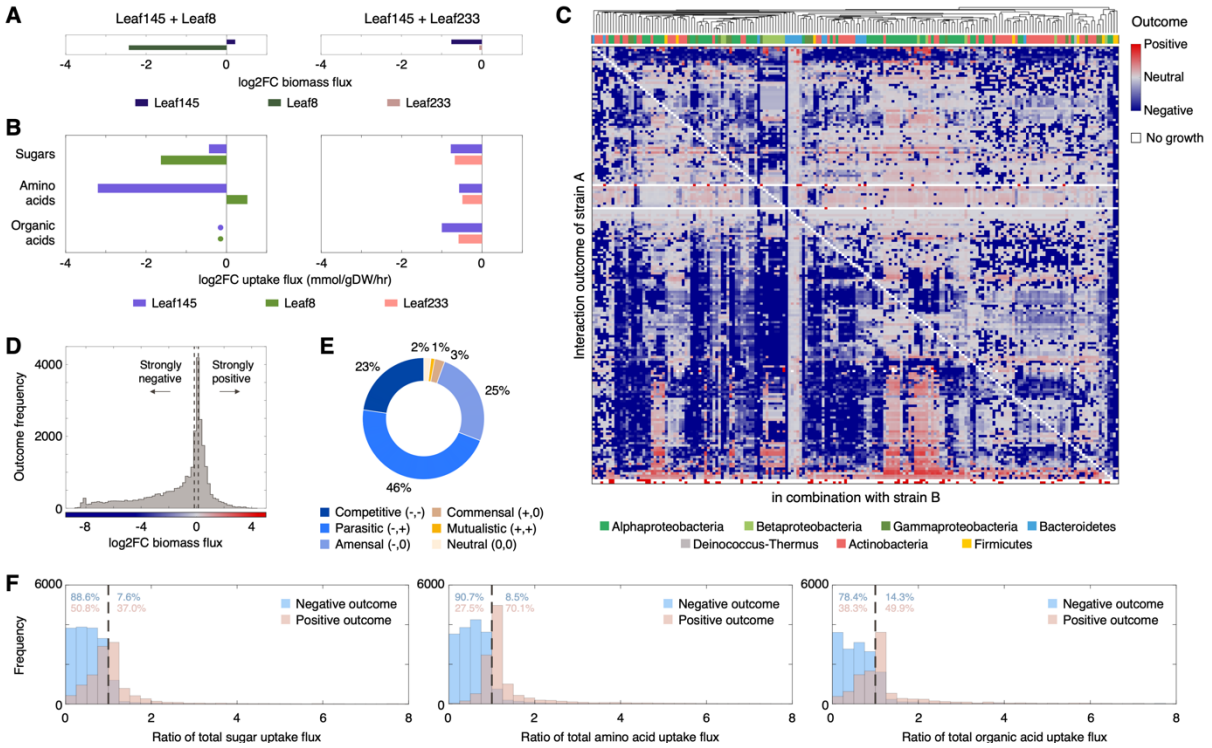

Fig. 5.

Model-predicted interaction outcomes and mechanisms. **A, B)** Log2 fold changes of biomass (A) and resource uptake (B) fluxes for two representative interactions validated in planta. Dots indicate absolute log2 fold changes of less than 0.05 mmol/gDW/hr. **C)** Predicted pairwise interaction outcomes between all 188 non-methylotrophic strains in the *At*-LSPHERE (n = 35,156 outcomes for 17,578 pairs). Hierarchical clustering was performed on interaction outcomes, with strain-specific phylogeny highlighted. White cells denote instances of no predicted growth in both mono- and coculture. **D)** Distribution of pairwise interaction outcomes (n = 35,156). Dashed lines separate outcomes in which a strain's predicted biomass flux in coculture was either: less than 90% of that in monoculture (strongly negative), within 10% of that in monoculture (neutral), or more than 110% of that in monoculture (strongly positive). **E)** Classification of pairwise ecological outcomes (n = 17,578). **F)** Distributions of flux ratios between resource uptake in coculture and monoculture, according to corresponding interaction outcome. Only simulations in which a strain achieved growth both in monoculture and coculture are considered (n = 28,316 outcomes). Differences between uptake rates of resource types provided in the simulated medium are highlighted for sugars (left), amino acids (center), and organic acids (right). Distributions of uptake fluxes are statistically significant for all three resource types ($p \ll 1 \times 10^{-10}$) as determined by one-tailed Mann-Whitney U-tests. For clarity, horizontal axes are truncated and show 98.8% of outcomes for sugars, 98.7% for amino acids, and 94.7% for organic acids. Dashed line at ratio of 1 separates instances of lower or higher uptake flux between coculture and monoculture with percentages highlighting the number of instances less than or greater than 1.

Science
AAAS

Supplementary Materials for

Metabolic interaction models recapitulate leaf microbiota ecology

Martin Schäfer, Alan R. Pacheco, Rahel Künzler, Miriam Bortfeld-Miller, Christopher M. Field, Evangelia Vayena, Vassily Hatzimanikatis, and Julia A. Vorholt
Correspondence to: jvorholt@ethz.ch

This PDF file includes:

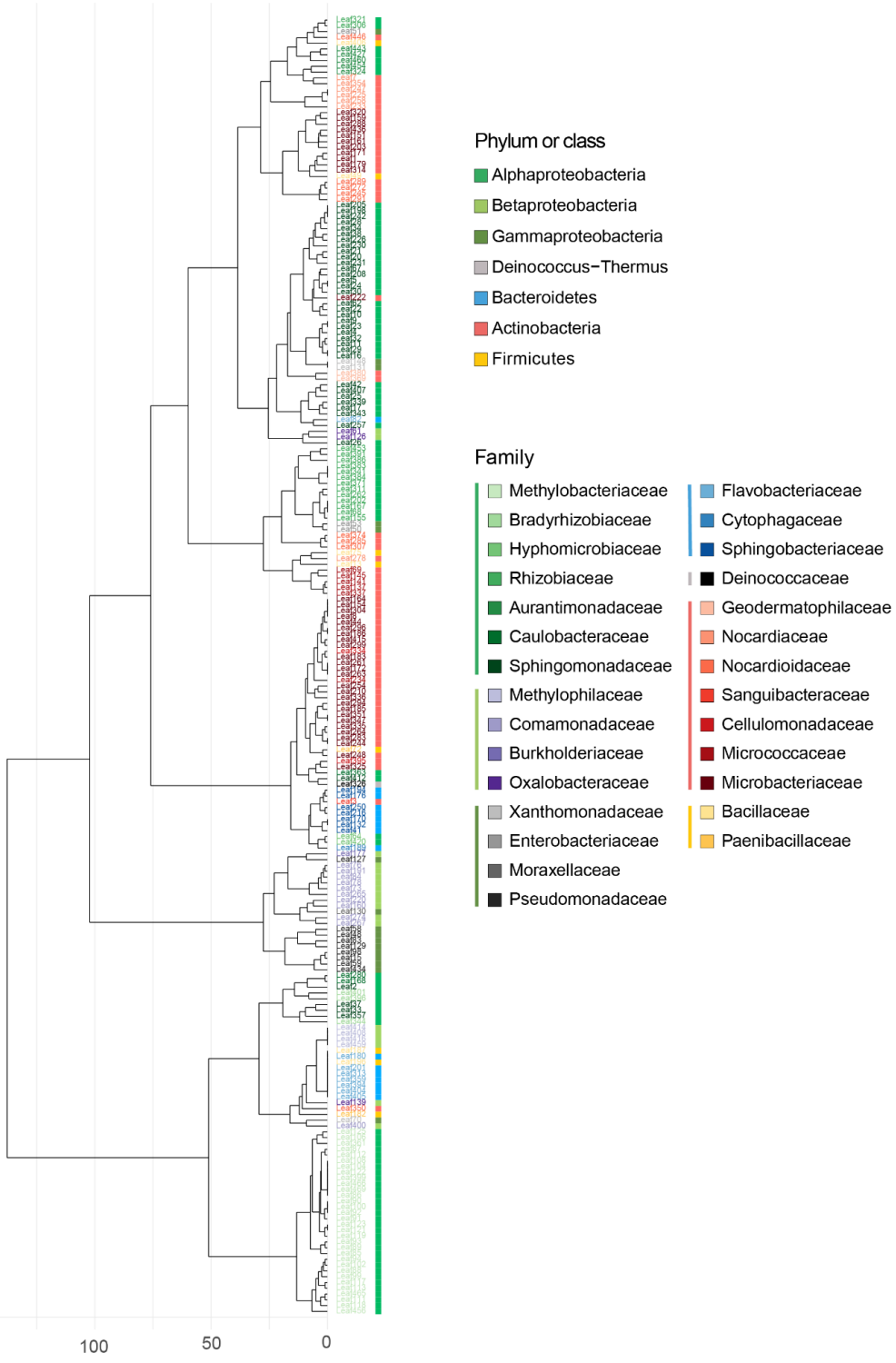

Fig. S1.

Hierarchical clustering of *At*-LSPHERE strains based on carbon source utilization profiles. Strains were clustered on Manhattan distances with Ward D2 method. Strain labels are color coded by bacterial family and the bar indicates the corresponding Phylum or Proteobacterium class.

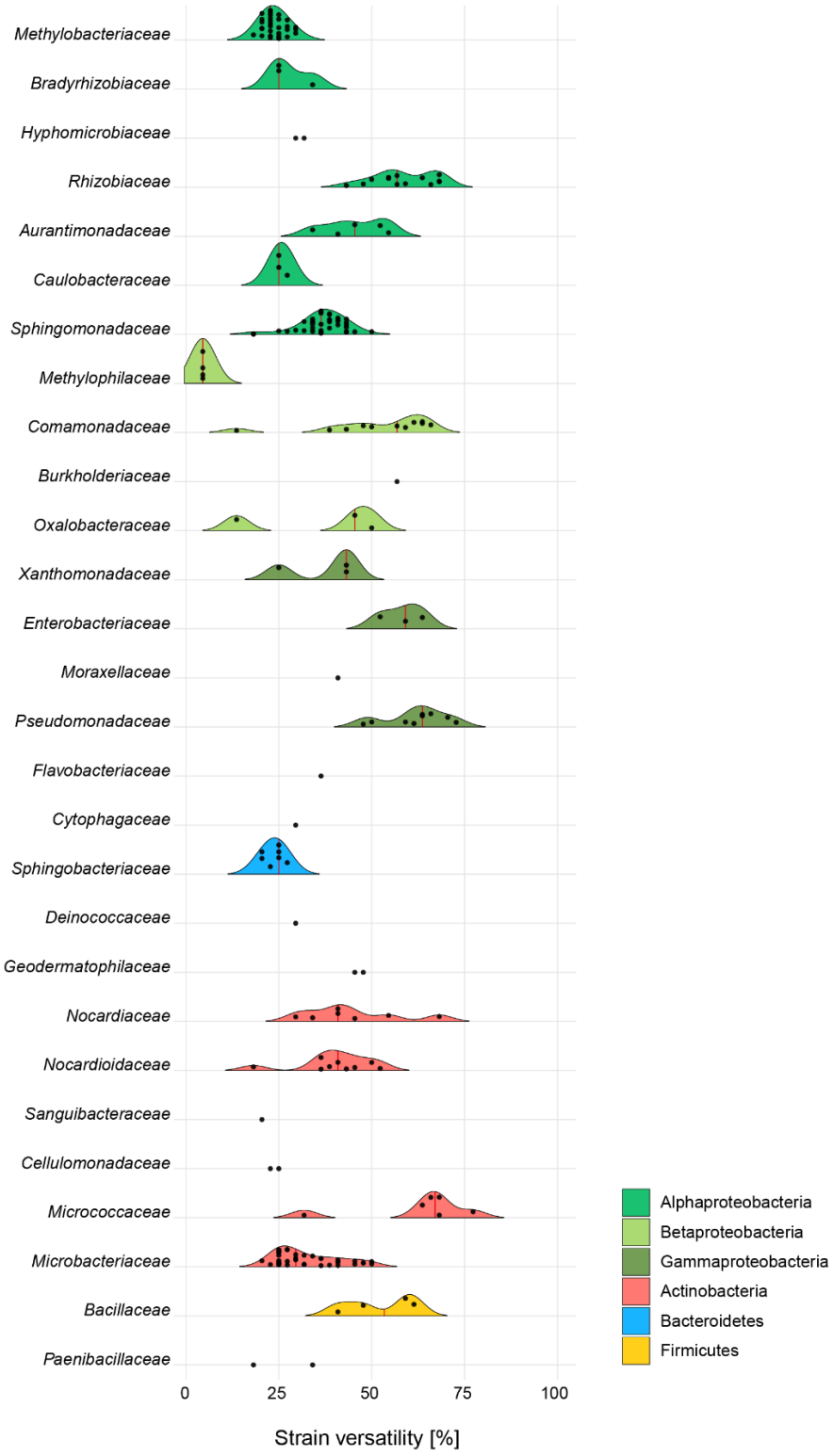

Fig. S2.

Density plots of family-level strain-specific versatilities. Black dots indicate individual values, and the red vertical line shows the median for each group. Fill colors represent phylum or Proteobacterium class.

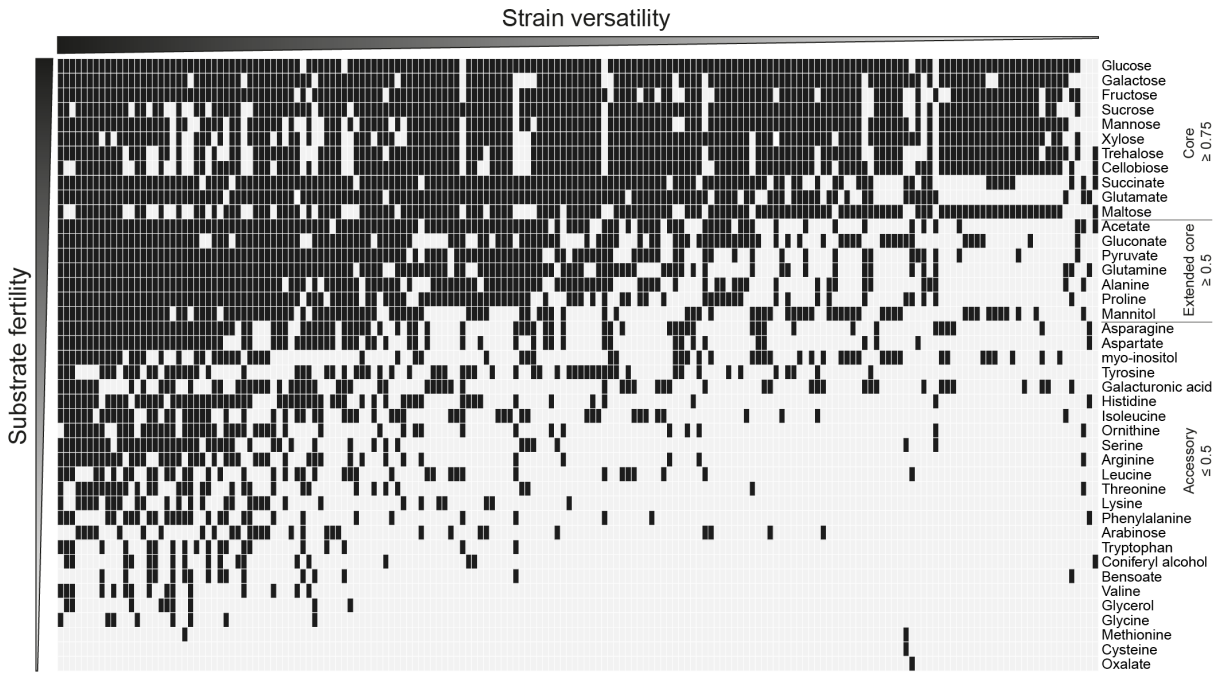

Fig. S3.

Carbon source utilization map of non-methylotrophic *At*-LSPHERE strains that experienced growth on at least one carbon source ($n = 179$). Fill color of the boxes indicate growth (black) or no growth (grey) for each strain on the x-axis on a given carbon source on the y-axis. The strains and carbon sources are sorted by decreasing versatility and substrate fertility, respectively.

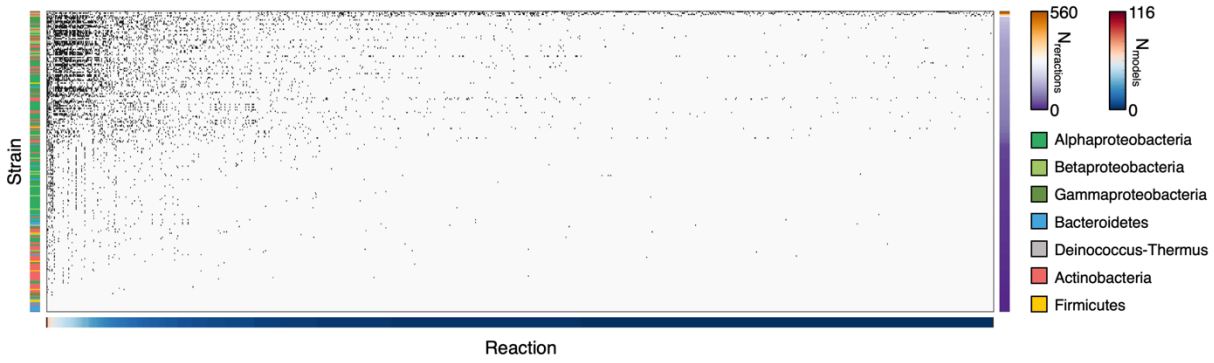

Fig. S4.

Summary of reactions added to draft models using NICEgame and additional curation. Black squares indicate addition of a reaction to the draft model of a given strain. Gap-filling resulted in a median of 23 reactions added to each draft model (IQR = 11 - 102). 220 out of 224 models had fewer than 200 reactions added, while only two models (*Rathayibacter* sp. Leaf167 and *Variovorax* sp. Leaf267) had more than 500 reactions added. 2,366 out of 5,231 total reactions were added to a model at least once, while only 1,336 (25.5%) reactions were added more than once. The top 5 gap-filled reactions (with corresponding EC number when available) were: CO_2 transporter, asparagine synthetase (6.3.1.1), O-succinylbenzoate-CoA ligase (6.2.1.26), calcium transporter (3.6.3.8), and O-succinylbenzoate-CoA synthase (4.2.1.113) (added to 116, 95, 73, 72, and 71 models respectively). A complete overview of gap-filled reactions per model is found in Table S3.

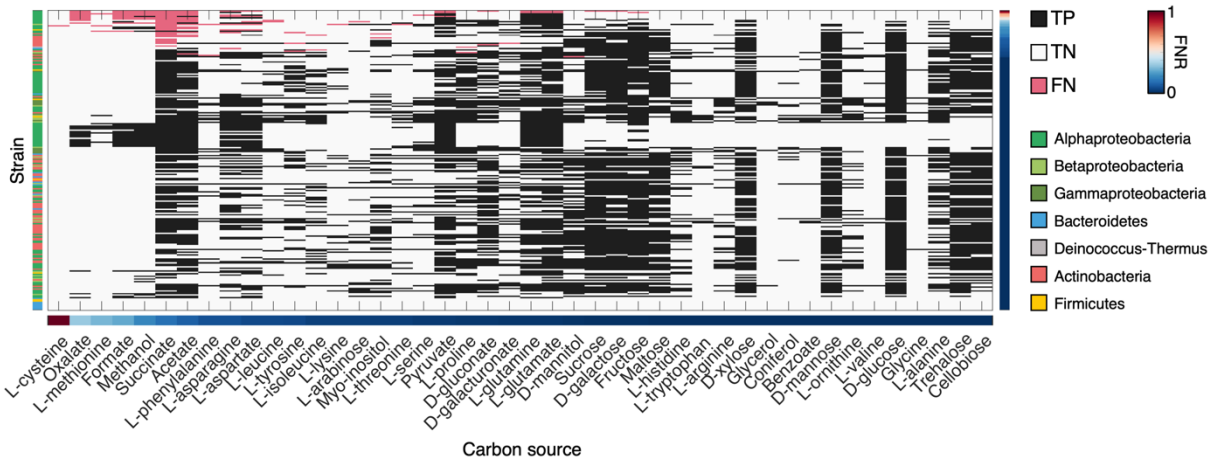

Fig. S5.

Mapping of strain- and carbon source-specific accuracies. Carbon sources and strains are sorted by false negative rate (FNR). TP, TN, and FN refer to true positive, true negative, and false negative, respectively.

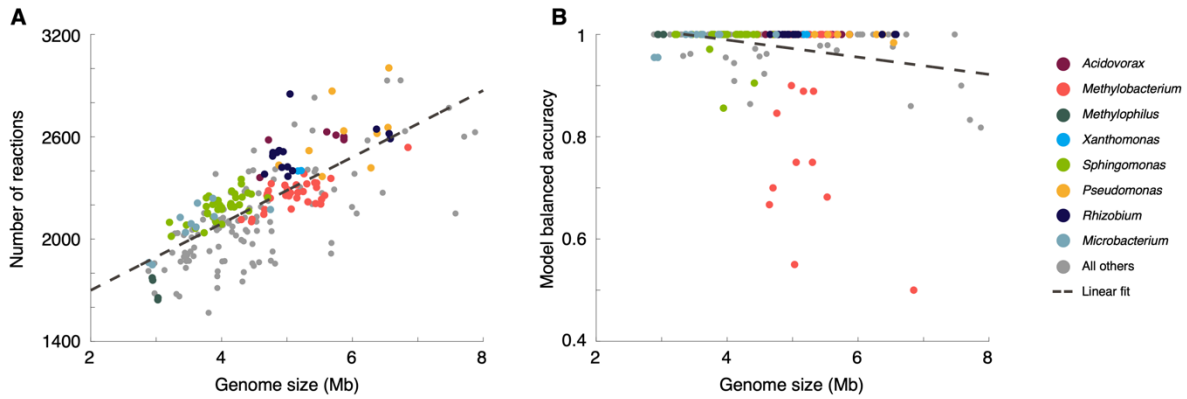

Fig. S6.

Comparison of model characteristics to genome size, with select genera highlighted. **A)** Correlation between genome size and model size (quantified by number of reactions). Linear model $R^2 = 0.54$, $P = 9.97 \times 10^{-39}$. **B)** Correlation between genome size and model balanced accuracy. Linear model $R^2 = 0.06$, $P = 2.08 \times 10^{-4}$.

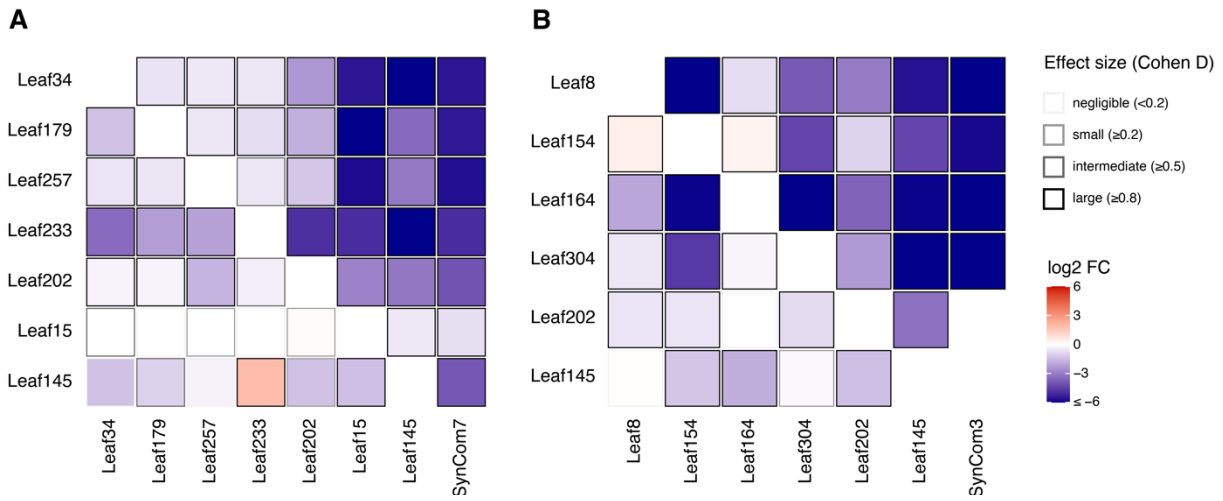

Fig. S7.

Interaction outcomes observed in shake flask experiments. **A, B)** Heatmaps showing the log2FCs (pairwise/SynCom inoculation vs monoculture) for each strain on the y-axis in combination with the strain or SynCom indicated on the x-axis based on absolute abundances obtained by CFU enumeration ($n = 4$ flasks per treatment). The color of the boxes reflects the observed log2FC and shade of the frames around the boxes denote the effect size (Cohen D).

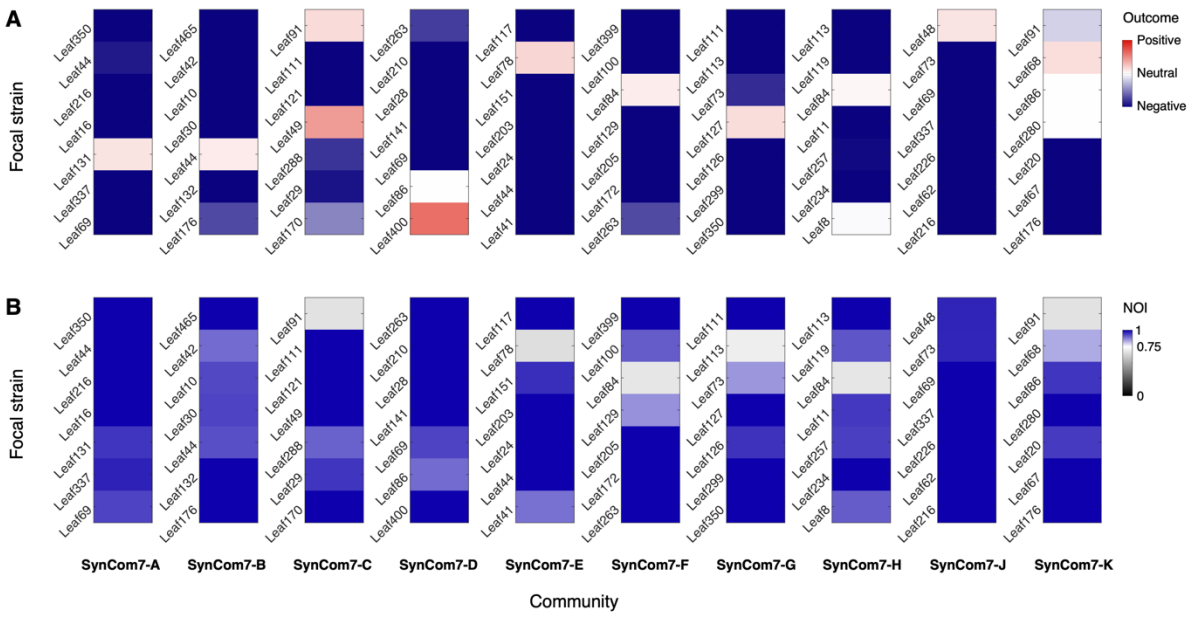

Fig. S8.

Interaction outcomes (A) and niche overlap indices (B) for strains in 10 random 7-member communities. As in the SynCom7 condition tested in silico and in planta (Fig. 4C, D), the interaction outcomes shown correspond to each focal strain within a community composed of all 7 strains. 80% of interactions resulted in negative outcomes for the focal strain, with 15% resulting in positive outcomes.

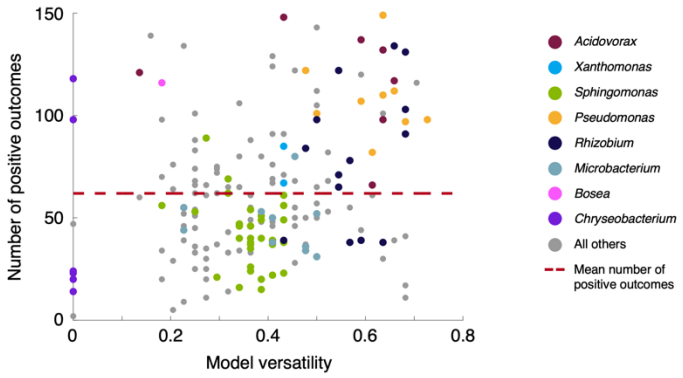

Fig. S9.

Relationship between predicted resource use versatility V for each model and frequency of positive interaction outcomes, with select genera highlighted. Mean number of positive outcomes = 61.9. Linear model $R^2 = 0.10$, $P = 7.25 \times 10^{-6}$ (trendline not shown).

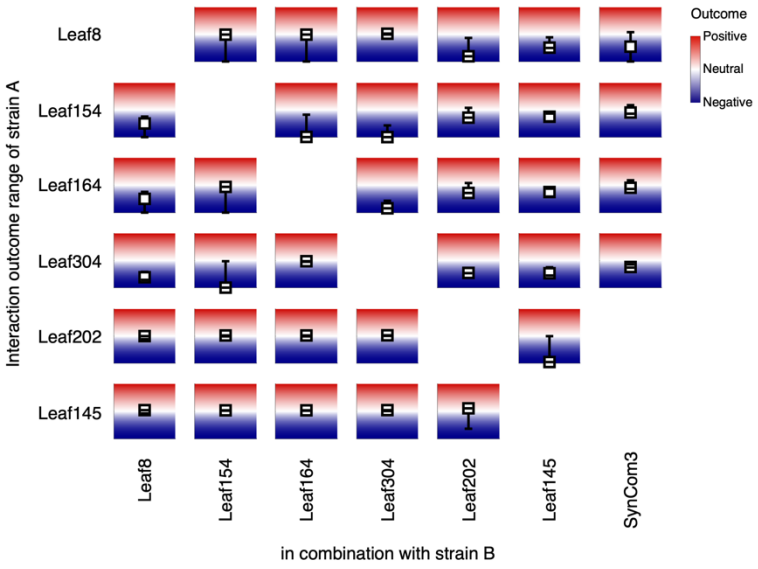

Fig. S10.

Representation of uncertainty in interaction predictions for 6-species experiments (Fig. 4E, F), which estimates the space of feasible interaction outcome directionalities for each strain using flux balance analysis. For each strain pair or community, we first set the sum of the biomass reactions of all organisms as the objective to be optimized. The strain-specific changes in biomass flux resulting from these optimizations are denoted by the white boxes and are equivalent to the outcomes shown in Fig. 4E. We then carried out a flux variability analysis to determine the species-specific biomass fluxes that would still result in a pairwise or community growth rate of at least 95% of the optimum. The range of strain-specific changes in biomass flux resulting from this analysis are represented by the whiskers.

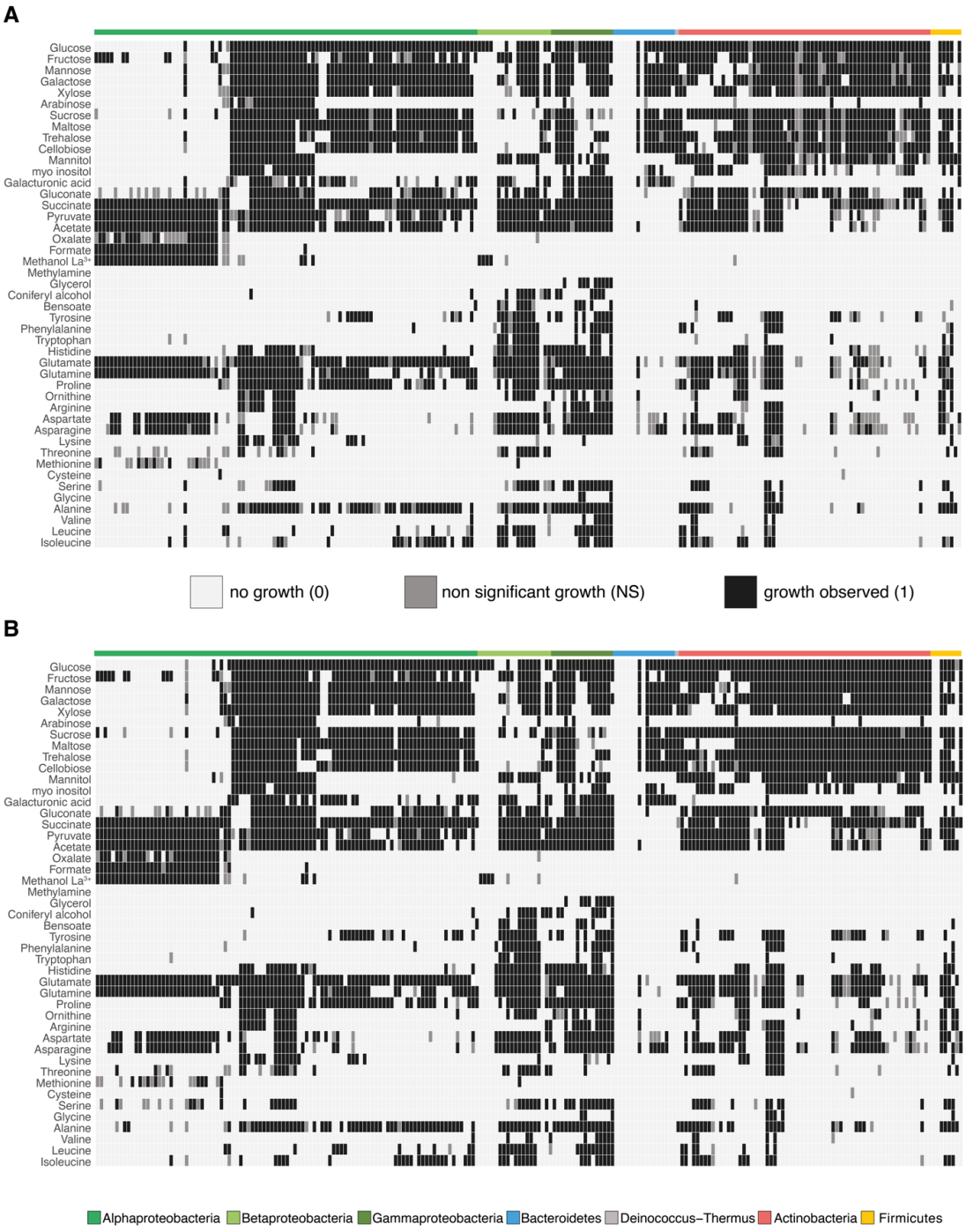

Fig. S11.

Carbon source utilization profiles of 224 *At*-LSPHERE strains when scored manually after seven days of growth (A) or when combining manual scoring with computational scoring through image analysis and reassessment of non-significant growth conditions after 10 days of growth (B). Fill color represents growth (black), no growth (light grey) or residual/non-significant growth (grey) for each strain on minimal medium agar plates containing a single carbon source indicated on the left. Strains are grouped by phylum or Proteobacterium class in the same order as in the legend.

Fig. S12.

Comparison of the carbon source utilization profiles obtained based on manual- and platescan software-based growth scoring. The fill color represents the overlap (light grey and black) and differences (purple and green shades) respectively between the two scoring methods. Strains are grouped by phylum or Proteobacterium class in the same order as in the legend.

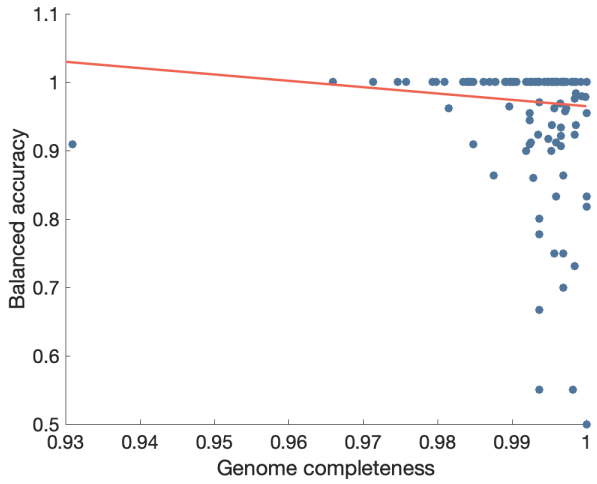

Fig. S13.
Relationship between model accuracy and completeness of underlying genome. Linear model $R^2 = 0.003, P = 0.201$.

Table S1 (separate file). Carbon sources used in in vitro screen.

Table S2 (separate file). Carbon source utilization profiles of 224 *At*-LSPHERE isolates.

Table S3 (separate file). Summary of reactions added to draft metabolic models during curation.

Table S4 (separate file). Accuracy statistics for genome-scale modeling interaction predictions.

Table S5 (separate file). Colony counts for in planta competition experiments.

Table S6 (separate file). Minimal medium composition for genome-scale modeling.

Table S7 (separate file). Carbon source utilization profiles of 56 *At*-LSPHERE isolate validation set.

Table S8 (separate file). Assessment of genome quality for strains.